Scalable Optical Architectures for Electronic Holography

by

Pierre St.-Hilaire

Master of Science (Physics)
Mc Gill University
1988

Submitted to the Program in Media Arts and Sciences,
School of Architecture and Planning,
in Partial Fulfillment of the Requirements for the Degree of

Doctor of Philosophy

at the
Massachusetts Institute of Technology
September 1994

Signature of the Author . .....
Pierre St-Hilaire
Program in Media Arts and Sciences
June 23, 1994

Certified By . . . . . .
Stephen A. Benton
Allen Professor of Media Technology
Program in Media Arts and Sciences
Thesis Supervisor

Accepted by . . . . .
Stephen A. Benton
Chairman
Departmental Committee on Graduate Students
Program in Media Arts and Sciences

Scalable Optical Architectures for Electronic Holography

by

Pierre St.-Hilaire

Submitted to the Program in Media Arts and Sciences,
School of Architecture and Planning, on June 23, 1994
in Partial Fulfillment of the Requirements for the Degree of
Doctor of Philosophy

Abstract

Holography has long been recognized as an effective way to convey the information of complex 3-dimensional structures such as those encountered in medical imaging, computer-aided design and navigation. However, attempts at implementing a real-time holographic display device have been hampered by the enormous space-bandwidth products required by such a task. I present here an approach that alleviates many of the problems encountered in previous attempts at real-time computer generated holography.

The basic idea underlying the MIT electronic holography display is the use of an acousto-optic modulator as a dynamic display medium and the synthesis of a large aperture by scanning the image of the modulator. The original implementation of the display is unsuitable for images larger than a few square centimeters, because the necessary optical space-bandwidth product become unmanageable by the electronic and optical subsystems. The goal of this thesis is to demonstrate that large displays can be implemented with available technologies if we break the space bandwidth product in small segments at both the image plane and Fourier plane, i.e. if we take a parallel approach.

In the image plane domain the display space-bandwidth product can be increased by simultaneously writing multiple acoustic columns on a single crystal and then optically multiplexing the

resulting holograms. I discuss the proper conditions under which the interline crosstalk remains acceptable and introduce a scanning geometry that allows for such a multiple channel operation. The Fourier domain can also be segmented in small domains, each being processed by a different scanning element. I describe the behavior of the image when such a segmentation in implemented and I then derive the conditions under which it can be effected without incurring significant image degradation.

I finally describe the implementation of these concepts into a large scale holographic display which includes the use of an array of 6 galvanometric scanners as the horizontal scanning element, two 18-channel acousto-optic Bragg cells working in tandem, and a bank of custom-designed high-bandwidth framebuffers. The application of the concept of parallelism has allowed a six-fold scale-up of the display, which now produces high quality images 150mm x 75 mm in frontal dimensions, with a 30 degrees view zone.

Thesis Supervisor: Professor Stephen A. Benton.

Title: Allen Professor of Media Technology, MIT Media Laboratory.

Scalable Optical Architectures for Electronic Holography

by

Pierre St.-Hilaire

The following people served on the comittee for this Dissertation

Committee Member .....

.....
Stephen A. Benton
Allen Professor of Media Technology
Program in Media Arts and Sciences
Thesis Supervisor

Committee Member .....

.....
V. Michael Bove Jr.
Associate Professor
Program in Media Arts and Sciences

Committee Member .....

.....
Cardinal Warde
Professor
Department of Electrical Engineering and Computer Science

To Louise

Acknowledgements

This project would not have been made feasible without the collective effort of a large number of people. The author wants to acknowledge the help and support of the following people:

Professor Stephen A. Benton (thesis adviser).

Mark Lucente and John Underkoffler (hologram computation).

John Watlington, Carlton J. Sparrell, Shawn Becker, and V. Michael Bove (Cheops Gods).

Wendy Plesniak (stereographic image computation).

Mike Halle (Unix God).

Michael Klug (who developped the holographic diffuser).

John D. Sutter and Ravikanth Pappu (members of the holovideo team).

Jeff Breidenbach, Uli Friedman, Derek Arias, Kevin J. Whitcomb, Brad Edelman, Rajeevan Amirtharajah (UROP's).

Bill Burling (help with the Kodak digital camera).

Linda Conte, Melissa Yoon, and Linda Peterson (staff members of the MIT Media Laboratory).

Phil Barrows of Cambridge Technology (technical support).

My parents.

My wife Louise.

Sophie Bernard, Terry Mc Lelland, Stephan Fitch, and Normand Thuot for moral support.

Research on the MIT holographic video system has been supported in part by US West Advanced Technologies Inc., the Defense Advanced Projects Research Agency (DARPA) through the Rome Air Development Center (RADC) of the Air Force System Command (under contract No. F30602-89-C-0022) and through the Naval Ordnance Station, Indian Head, Maryland (under contract No.

N00174-91-C0117), and by the Television of Tomorrow research consortium of the Media Laboratory, MIT.

TABLE OF CONTENTS

I INTRODUCTION

1.1 The need for advanced visual interfaces

1.1.1 Graphical user interfaces

A cliche often used when describing the progress of computing devices goes like this: If cars had followed the same evolution curve that computers have done, a contemporary automobile would cost a dollar and could circle the earth in an hour using a few cents worth of gasoline. Applying the same metaphor to computer display devices, however, would likely find us at the wheel of a 1940's vintage Buick.

The fact is, there has been little conceptual advances in display technologies since the advent of television in the 1940's. The NTSC standard adopted at that time specified a display resolution of 480 scan lines and about 640 pixels horizontally (It should be noted that NTSC images are not sampled in the horizontal direction, but the 640 pixels figure is a commonly used approximation). Today's high end computer terminals offer color images having 1280 pixels horizontally and 1024 scan lines. This corresponds to a factor of 4 improvement over more than a half century. A few displays offer resolutions in the 2000 x 2000 range, which represents a factor of 13 over NTSC - a figure that hardly compares to the evolution of computing devices.

There is nowadays a considerable effort aimed at the development and manufacture of a new generation of flat panel displays. Such an effort is spurred by the enormous market predicted for such devices in portable computers and high definition television (HDTV). But the overwhelming fraction of this effort is aimed at devices achieving characteristics similar to todays CRT's - only in a flatter, more efficient, and hopefully less expensive manner.

There is, however, a real need for display devices that could go beyond what we have become accustomed to. Conventional display devices offer only a puny fraction of the information that

can be processed by the human visual system. Compare this situation to the field of acoustics, where digital recording devices and modern loudspeakers can offer sound of an almost lifelike realism. With respect to these, even the most advanced high resolution displays now in use would fare about as well as Edison's first recordings on wax cylinders.

This situation could be accommodated when the output of digital devices consisted in little more than strings of letters and numbers. However, displaying the enormous amount of data being processed by today's computers offers a formidable challenge from both the technical and human interface perspectives. This challenge is unlikely to be resolved without bold and innovative approaches to the problem of scientific visualization.

Researchers at the MIT Media Laboratory Visible Language Workshop (VLW) under the supervision of the late Muriel Cooper have taken the first steps towards a whole new paradigm in the design, organization, and display of complex multidimensional data sets. These researchers well understood that conventional monitors and user interfaces designs were inadequate in conveying massive amounts of data. One of their early tasks thus consisted in optically tiling three high resolution monitors to achieve a display having an effective resolution of 6000 x 2000 pixels[61]. They then designed graphical user interfaces that used three dimensional metaphors such as transparency, blur, layering, and zoom to navigate through this "information landscape[60]". Their early work clearly demonstrate that using a three dimensional representation can considerably augment the human brain in accessing and assimilating large amounts of information.

The VLW researchers are now using a commercially available stereographic display (the Crystal Eye, manufactured by Stereographics Corp., San Rafael, CA) to evaluate their three dimensional interfaces. Other groups performing related work prefer to use head mounted displays which offer a wider field of view but a lesser resolution. The limitations of these technologies are quite evident for researchers in the field. Stereographic displays render a scene from a single viewer perspective. They are thus incapable of rendering motion parallax, which is one of the most important depth cues that the human brain uses to extract depth from a scene. Attempts at simu-

lating motion parallax by tracking the position of the viewer's head invariably run into a significant time lag due to the tracking, image rendering, framebuffer loading, and screen refresh intervals. Moreover, these devices require the viewer to wear goggles that are often quite cumbersome. Finally, none of these technologies present the feature of ocular accomodation, another depth cue used by the brain to extract the range of nearby objects. The VLW graphical interface, which makes use of image blur to simulate different depth planes, would obviously considerably benefit from a device that could intrinsically reproduce arbitrary focal planes.

A few experiments in which multiple focal planes were used to display layered text and images were attempted by Kenneth M. Carson at the MIT Media Laboratory[65]. Carson used a varifocal mirror made of an aluminized membrane driven by a loudspeaker to image the phosphors of a CRT at different planes. Early results clearly demonstrated the potential of volumetric imaging technologies, despite the fact that the display acted like a large subwoofer and that varifocal displays cannot reproduce occlusion.

1.1.2 Vision studies

In the late 1980's Edward H. Adelson of the Massachusetts Institute of Technology introduced the concept of *plenoptic function* to describe the structure of the information in the light impinging on an observer[62]. The plenoptic function describes everything that can be seen, hence its name (from *plenus*, complete, and *optic*). The parameters of the plenoptic function thus include the light intensity distribution at the viewer's pupil, as well as the wavelength, viewer position, and, in the case of moving images, time. Adelson's thesis is that the human brain extracts the salient features of this function principally by using sets of oriented filters in the visual cortex. Indeed such structures have been found by various research groups[63].

In principle, determining the exact response of these filters opens the possibility of presenting the viewer with a prefiltered version of the plenoptic function. The modified function would be undistinguishable from the original, although requiring considerably fewer amount of data to repre-

sent. This determination presents obvious applications in image compression, apart from its fundamental contribution to vision science.

The determination of the total processing bandwidth of the human visual system is considerably complicated by the fact that these cortical filtering structures are multidimensional. Moreover, conventional displays can present only a very small fraction of the plenoptic function to the observer. A technology that could be used to convey the complete plenoptic function would represent a major advance in the study of human vision.

Conveying the entire plenoptic function to an observer implies an arbitrary degree of control over the wavefronts reaching the eye (excluding absolute phase and polarization, to which the human visual system is not sensitive), and obviously requires the processing of large amounts of data. From early on holography was considered as a most likely candidate for this task, since in theory a hologram allows the reconstruction of an arbitrary wavefront over an extended portion of space. Despite a period of enthusiasm in the early 1960's, however, display holography has yet to fulfill its promises. Indeed, numerous researchers have stated that the holy grail of display technology, namely a holographic display capable of a perfect scene realism, is a technological impossibility. The goal of this thesis is to demonstrate that this is not so. Digital holographic displays have been demonstrated and can be scaled to useful sizes by adopting the appropriate optical architectures.

1.2 The bandwidth bottleneck

Although conventional display holograms can produce bright, full-color images of high resolution and a large range of depths, they are static, and cannot be altered electronically as can a typical two-dimensional display. Any use of three-dimensional data for interactive, animated, or real-time display is commonly limited to a two dimensional rendering and display on a cathode-ray tube (CRT). The possibility of a real-time holographic display has only recently emerged due to advances in computers and computational methods, which allow for the rapid (seemingly real-time) computing of a holographic representation of a given set of three-dimensional data, as well

as new electro-optical technologies for their display.

Up to a few years ago the interactive display of holograms was deemed impossible by a number of researchers due to the formidable technical obstacles any such endeavor would need to overcome. All those obstacles result from the very large amount of information necessary to convey an holographic image at either the computational, transmission,or display step. A simple calculation easily illustrates the extent of the problem. The information content of a holographic image is readily calculated if we start from the grating equation:

$$\lambda f_h = \sin\theta \tag{1.1}$$

Where f_h is the maximum spatial frequency of the hologram fringes, λ is the wavelength of the diffracted light and θ is the angular width of the view zone.

According to the sampling theorem, the minimum sampling frequency f_s required to generate or digitally transmit the hologram is:

$$f_s = 2f_h \tag{1.2}$$

so that the number N of samples required for a 1-dimensional hologram of width d is:

$$N = df_s = \frac{2d\sin\theta}{\lambda} \tag{1.3}$$

The total number N_t of samples required for a hologram with only horizontal parallax and with a vertical resolution of l lines is thus:

$$N_t = lN_s = \frac{2dl\sin\theta}{\lambda} \tag{1.4}$$

For a full parallax hologram of height w we have :

$$N_t = \frac{4dw \sin^2\theta}{\lambda^2} \tag{1.5}$$

The information content of a typical hologram is thus several orders of magnitude larger than that of a two-dimensional image, such as the image on a CRT display. From equation (1.5), a full parallax hologram of dimensions 100 mm by 100 mm and a maximum diffraction angle of 30 degrees contains approximately 25 billion samples of information - all for a single frame. In order to update such an image with 8-bit resolution at a rate of 60 frames/second, a data rate of 12 Terabits/sec would be required for transmission of the hologram. This bandwidth is well beyond the range of current technology. A number of steps are clearly necessary before any electronic holography display can be implemented.

1.3 Information content reduction strategies

1.3.1 Elimination of horizontal parallax

The human visual system extracts depth information in a scene mostly by virtue of its horizontal parallax, a feature that has been applied in stereoscopic and lenticular displays. The elimination of vertical parallax has also been exploited by Benton in the generation of white light viewable holograms[14]. A horizontal parallax only (HPO) hologram represents a scene from a single vertical perspective only and the number of holo-lines is only matched to the vertical image resolution. The vertical pitch of a HPO hologram thus has typical values of a few lines per mm, as opposed to about 1000 for full parallax images. As a result, a two orders of magnitude gain in information content is typically achieved. For instance, if we consider our previous example with a vertical pitch of 4 lines/mm, the application of Equation (1.4) gives a total number of samples of 63 million per frame.

Eliminating the vertical parallax results in considerable savings in display complexity. Indeed, the display technology researched at the MIT media Laboratory, which relies on the application of

one-dimensional transforms, would be unapplicable to full parallax displays. Because the vertical focal plane is fixed and the horizontal focus is variable, HPO holograms exhibit some astigmatism[14]. This astigmatism can be kept to a minimum if the vertical focal plane coincides with the middle plane of the image. Extensive experience with rainbow holograms shows that this astigmatism remains virtually unnoticeable even for fairly deep objects.

1.3.2 Reduction of horizontal display resolution

A conventional hologram can image features of the order of a few wavelengths, while at a usual viewing distance (say 600 mm) the human visual system will be unable to resolve features smaller than 200 micrometers (corresponding to a 1 minute of arc angular extent). This property has been exploited by Lucente who obtained considerable computational savings by precomputing holographic fringes and then accessing them using a look up table[19]. The savings as far as display technology is concerned are less obvious, however, since the sample size at the hologram plane is determined by the maximum angular extent of the scene as determined by equations (1.1) and (1.2).

Another consequence of the limited resolution of the human eye is that it is possible to sequentially display sections of the hologram without perceptible degradation if the proper conditions are met. Chapter II will demonstrate how this property is fundamental to the present implementation of the MIT display.

1.3.3 Reduction of image size and horizontal viewing angle

Again referring to equations (1.4) and (1.5), it becomes obvious that the easiest way to reduce the information content of a hologram is to reduce the size and viewing angle of the image. The horizontal viewing angle, however, should be large enough so that both eyes of the observer fit within the view zone. Assuming a viewing distance of 600 mm and an intraocular distance of 65 mm thus results in a minimum angle of 6.2 degrees. In practice a certain amount of "look around" is also

necessary to provide the horizontal parallax information that is an important depth cue in human vision. Allowing for a lateral translation of the observer by an amount equal to the intraocular distance doubles the horizontal view angle to a value of 12.4 degrees. Experiments performed on the MIT display confirm that this value results in acceptable images, although this falls short of the 45 degrees view zone more typical of conventional display holograms.

If the horizontal extent of the image is limited to 50 mm and we assume a HPO hologram with 100 lines of vertical resolution and a horizontal view zone of 12 degrees, equation (1.4) results in a number of samples of 3.3 million per frame. This figure is compatible with the performance of commercially available frame buffers.

1.4 Historical background

1.4.1 Related experiments

A large body of literature exists concerning the computer generation of holograms[9,10] but few attempts have been made at displaying those at video-like frame rates. Holograms displayed using present generation liquid crystal displays (LCD's) or magnetooptic light valves have a space-bandwidth product which is too small by two orders of magnitude to qualify as "display holograms".

The first attempts to display computer generated holograms in real time with a spatial light modulator were made at the California Institute of Technology in the mid 1980's by Psaltis *et al*[48] using a magneto-optic spatial light modulator. Later on the same group repeated the experiment with an LCD[49]. In both cases the low pixel count of the devices (128 x 128 for the magneto-optic device, 100 x 100 for the LCD) limited the experiments to a proof of principle.

More recent experiments on holographic displays using LCD's have been implemented in Japan by Hashimoto *et al.*[37]. An active matrix LCD display was used to modulate the phase of an colli-

mated HeNe laser beam. The images obtained by this group, however, were quite noisy and exhibited a very low space bandwidth product due to the limited resolution of the LCD. The same group is still active in the domain and is now working in the development of very high pixel count LCD's for use in holographic applications. LCD's still have a long way to go before they can be considered for practical aplications in real time display holography, but they hold the promise of flat panel displays and are rapidly improving.

A different approach at synthesizing three dimensional images is being attempted by Kulick et al. at the University of Alabama. Rather than attempting to generate actual micron-sized fringes, their approach is to precompute a set of basis fringes that are then modulated as a whole by a LCD panel. The images generated by this scheme are thus closely related to holographic stereograms. No practical device has yet been manufactured by this group, although the very preliminary work done so far seems encouraging.

Another research effort closely related to the goals of this thesis (namely, the display of reasonably good quality moving holograms) was the one of Goetz *et al.*[29], which used scanned laser beams to generate holograms of points in space using a thermoplastic recording material. The authors were hoping to achieve television-quality images and refresh rates of around 1 frame per second. It is interesting to note that while those authors were using AOM's as light modulators, the actual display medium was a thermoplastic sheet. The main problems encountered were due to the limited frequency response and high noise of this thermoplastic. Unfortunately, no subsequent reports followed the original publication.

1.4.2 The MIT holographic video project

Experiments on electronic holography were started at MIT in 1987 by Joel S. Kollin (then a MS student at the MIT Media Laboratory) and Professor Stephen A. Benton with initial funding provided by the U.S. West Corporation[27,55,59]. John S. Underkoffler, then an undergraduate student at MIT, computed the original fringe patterns using the newly acquired CM1 supercomputer from Think-

ing Machines Corporation.

Kollin and Benton came up with the original concept behind the MIT technology, namely the use of a scanned apertured Bragg cell as the display medium. It was only later that a bibliographical search uncovered the use of an almost identical geometry for the projection of television images developped in the late 1930's. The so-called Scophony projector was developed principally by J.H. Jeffree and was once considered a serious contender for the display of television images[16,57]. Unfortunately, it could not compete with the CRT which was already a well developped technology.

Further bibliographical investigations uncovered the fact that the use of a Scophony-type geometry had indeed been proposed at Xerox by Richard V. Johnson for the projection of three dimensional images[56]. Johnson proposed the use of programmable chirp filters to alter the focal plane of the image being writtten on a Bragg cell, an approach that is rather unpractical when compared to the numerical synthesis of holographic fringes. Johnson also did not seem to be aware that good three dimensional images could be achieved with horizontal parallax only holograms. Still, it is puzzling that no more publications came out from Xerox on this topic.

Considerable technical difficulties prevented the initial researchers from displaying images with the system under development. Indeed it was not until the summer of 1989 that simple geometric patterns with a vertical resolution of 8 scan lines could be convincingly demonstrated by the author of this thesis. Following this demonstration a U.S. patent was applied for in April 1990 and awarded in 1992[58].

Rapid progress followed the initial demonstration. A display exhibiting 192 horizontal scan lines was demonstrated in 1990[25] and color images were achieved in 1991[40]. It was then decided to experiment with scaling up the technology, an endeavour that led to this doctoral dissertation. The first results on the scaled up technology were presented in 1992[3] and by early 1994 we were able to display high quality images 150 mm across.

II FUNDAMENTAL CONCEPTS

2.1 Overall description of the first-generation MIT display

The fundamental idea behind the MIT electronic holography display is the use of an acousto-optic modulator (AOM) as the medium upon which the holograms are written[1,3]. The AOM consists of a single transparent TeO_2 crystal operated in the slow shear mode. At one end of the crystal is an ultrasonic transducer, which converts the electrical holographic information signal to a shear wave that is launched down the crystal. As the shear wave propagates, the regions of greater elastic shear present a modulated index of refraction to the optical beam, which passes at the Bragg angle with respect to the acoustic wave. The optical beam thus emerges from the crystal with a relative phase-difference pattern across its width that is proportional to the instantaneous amplitude of the shear wave along the length of the crystal. This complex fringe pattern transfers the computer-generated hologram (CGH) data to the optical beam. The crystal has an aperture time (width / sound speed) of 40 microseconds and a space bandwidth product (max cycles / mm x aperture width) of 2000. Its operating RF spectrum ranges from 50 to 100 MHz. Because its total angle of diffraction range is only 3 degrees, optical demagnification is needed to bring the viewing angle to a more acceptable value (typically 15 degrees).

Figure 2.1 shows the electro-optical portion of the display. A widened beam of coherent light is phase modulated by the input CGH data-stream in the AOM, and assembled into the image of the CGH by the scanning system. A 10mW HeNe laser is used as a coherent source of monochromatic red light (632.8 nm wavelength). The beam is spatially filtered, expanded, and collimated using a microscope objective, a pinhole, and a collimating lens. A horizontal slit-shaped portion of this beam passes through the AOM, producing a diffracted order, which represents a portion of one line of the hologram. In the AOM, the fringes propagate at a rate of 617 meters/second, which is the speed of shear waves in the TeO_2 crystal. Therefore, the diffracted image also moves (from left to

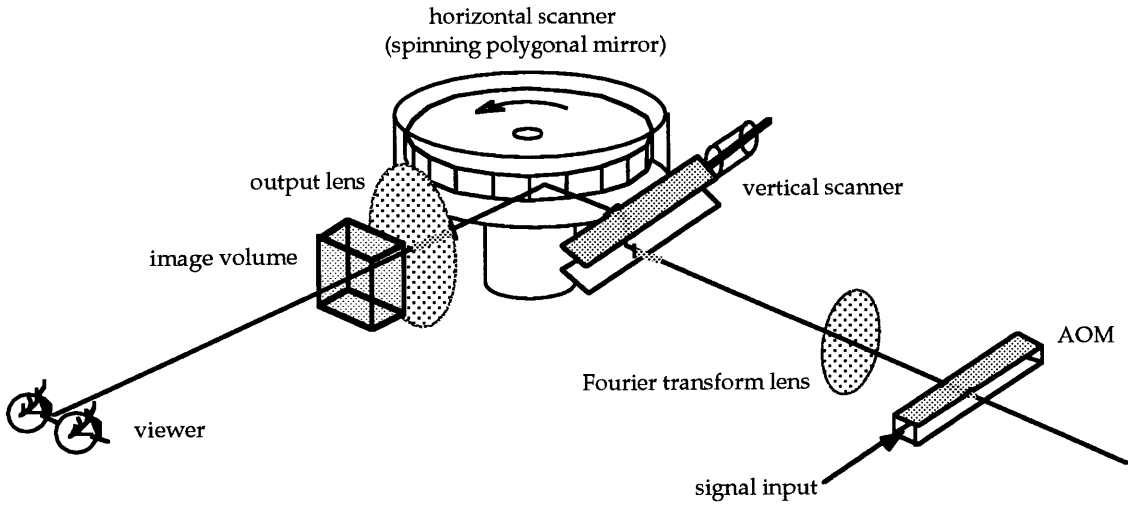

Figure 2.1 Electro-optical section of the original MIT holographic display. The vertical lenses have been omitted for clarity

right) at this rate. In order to make the image appear stationary, a spinning polygonal mirror is used to scan the image of the AOM horizontally in the opposite direction. The horizontal scan also acts to multiplex the image of the crystal, creating a virtual crystal that is exactly as long as one line of the CGH. This multiplexing is necessary because the crystal's time-bandwidth product is typically at least an order of magnitude smaller than the time-bandwith product of a single hologram line. We can thus think of our CGH as a narrow slit being displaced along a much wider hologram. This situation is very similar to the synthetic aperture radar (SAR) case where a narrow antenna is linearly and coherently scanned to give an effective aperture equal to the scan length[64], the main difference being that we are generating a wavefront instead of recording one (thus the name Synthetic Aperture Holography that is sometimes used to describe this concept). Another difference between our system and SAR is that our detector (the human eye) is an incoherent imaging device, being sensitive only to the intensity of the incoming light. This characteristic of the eye prevents the synthetic apertured hologram from displaying superresolved images, as is the case for SAR.

The vertical deflection is provided by a closed loop galvanometric scanner. The net effect is that of a small horizontal-parallax hologram being scanned in a raster fashion much like the electron beam in a CRT display. History-minded readers may note that the display exhibits many similarities

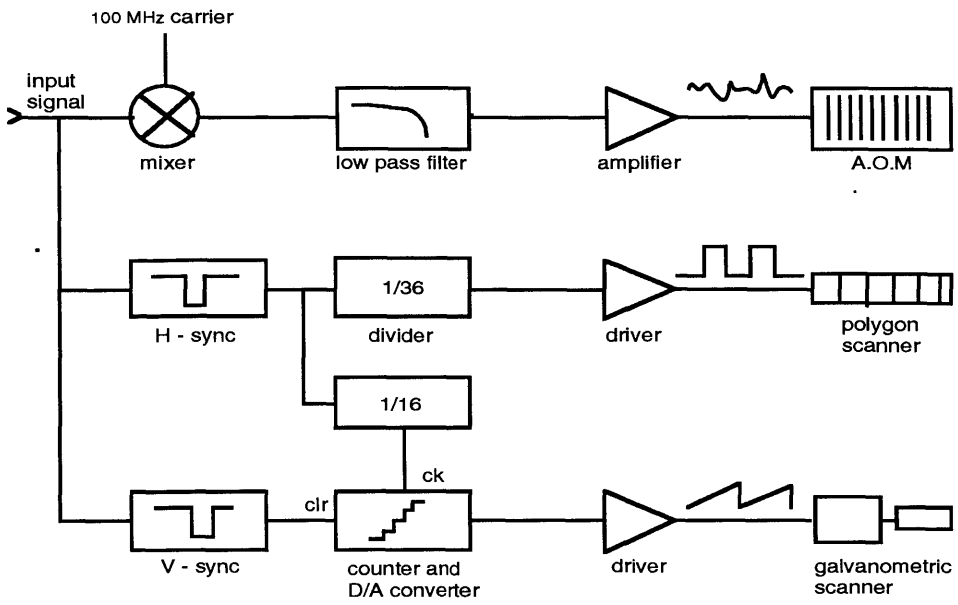

Figure 2.2 Block diagram of the first generation display electronics

with the Scophony system introduced in the 1930's for the projection of two-dimensional television images[16].

Computation of the images is done on a massively parallel supercomputer (Thinking Machines Corp. model CM2) using algorithms developed at our laboratory[19]. After computation the holographic information is sent to a high resolution frame buffer and converted to a signal having the same bandwidth as the AOM. This signal is then upconverted to the AOM operating frequency range by mixing it with a 100 MHz carrier and filtered to keep only the lower sideband. It is then amplified and used to drive the AOM.

The operation of the display requires a precise synchronization between the various parts of the system (polygonal mirror, galvanometric mirror and frame buffer), which is provided by the circuit of Figure 2.2. This circuit derives all the necessary drive signals from the horizontal and vertical sync pulses of the frame buffer .

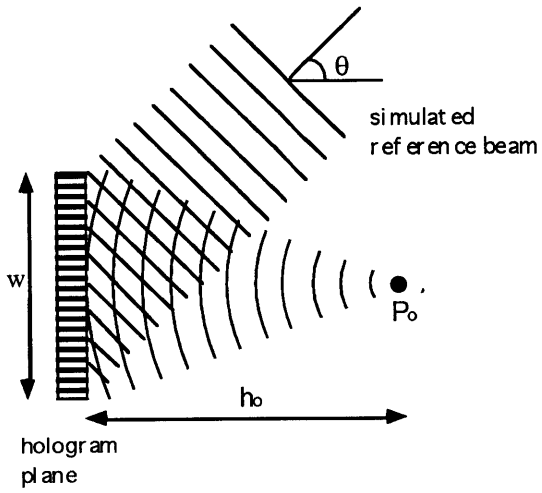

Figure 2.3 Hologram geometry for the computation of a single point. The fringe pattern is sampled at the hologram plane.

2.2 Mathematical optics of synthetic aperture holograms

2.2.1 The AOM as a Dynamic Hologram

Because of their wide bandwidth and dynamic range, Bragg cells have found many applications as elements of optical processors[20,21]. The optical processing community usually uses the formalism of linear systems theory to describe the operation of these devices. It will be much easier in the course of this section to treat the signal propagating on the AOM as a dynamic hologram rather than as an arbitrary waveform. This description also closely corresponds to the actual physical phenomenon we are trying to reproduce, namely three-dimentional imaging. Let us say that the object we want to display is a single point. At the computation step the corresponding geometry is shown in Figure 2.3. The "hologram" plane is at a distance h_0 from the point P_0 and the simulated wavelength corresponds to the wavelength eventually used for display (usually 633 nm). The maximum spatial frequency of the fringes is related to the maximum viewing angle by equation (1.1). During playback, the hologram information is launched at one end of the crystal as a series of radio-frequency shear waves. The wavelength Λ of these waves is related to the speed of sound V of the crystal and the RF frequency F by the equation:

$$\Lambda F = V \tag{2.1}$$

Usually, Λ is longer than the original fringe spacing Λ_f. The playback hologram will thus have correspondingly lower spatial frequencies with the following consequences:

- The holographic image will be magnified along the x-axis by a factor equal to Λ_f
- The maximum view angle will be reduced by the factor Λ / Λ_f.
- The image will be magnified along the z-axis by the factor $(\Lambda / \Lambda_f)^2$.
- The image will be at a distance $d_0 = h_0 (\Lambda / \Lambda_f)^2$ from the crystal plane.
- The image will move along the x-axis at the speed V.

Because the longitudinal and transverse magnification are different, the image will exhibit some distortion since it is elongated along the axis of highest magnification. For example, a sphere will be mapped into an ellipsoid.

2.2.2 Synthetic aperture displays - the general case

It is clear that viewing the image corresponding to the information being written on the Bragg cell requires a system that can compensate for the rapidly moving diffraction pattern. I propose to analyze a general class of optical systems for this purpose. The basic components of this geometry consist of the Bragg cell, an input lens L_1, an angular scanning element G, and an output lens L_2 (Figure 2.4). The scanning element rotates at an angular rate ω which is usually determined by the period of a scan line. This type of optical system was first proposed by J.H. Jeffree in 1936 for the projection of television images (Scophony system). For this reason it is sometimes described as the "Scophony geometry." This geometry has also been investigated in the late 70's for use in data recording[52], but as display devices Scophony-type video projectors could never be made to compete economically against CRT's. Some modern laser printers are based on a variation of this design.

We want to determine the conditions under which a fringe pattern corresponding to a single point

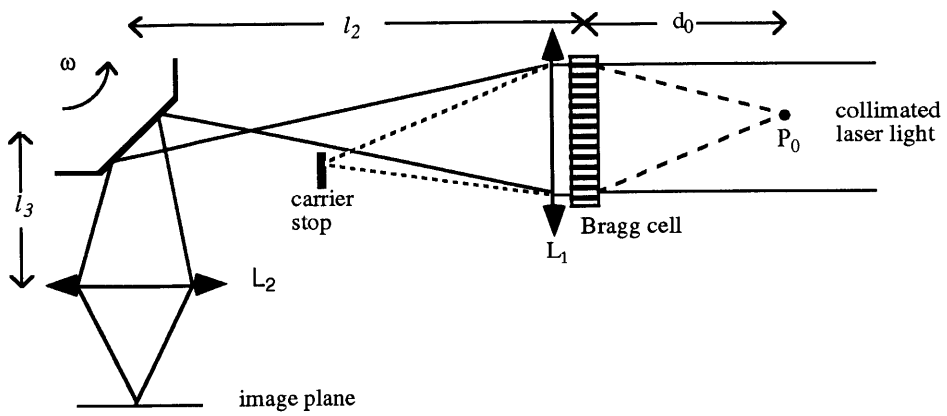

Figure 2.4 Horizontal geometry for the general case.

will be mapped into a stable image free of aberrations. A partial analysis using a conventional geometrical approach was presented in ref. 2. A more elegant treatment which uses an extension of the well known ABCD matrix description is described in Appendix A. I will only give the general results in this section.

Usually V is a constant dictated be the acousto-optic material and ω is determined by the display frame rate. This leaves l_2 and l_3 as independent parameters that can be manipulated to get a correct image. For the image to be stable with respect to time, l_2 has to obey the condition:

$$l_2 = \frac{f_1(2d_0\omega + V)}{2\omega(d_0 + f_1)} \tag{2.2}$$

Where f_1 and f_2 denote the focal lengths of lenses L_1 and L_2 respectively. For the spatial frequencies (corresponding to the directions from which the image is visible) to be stable with time the following condition has also to be followed:

$$l_3 = f_2 + \frac{V(f_1 - l_2)}{V - 2\omega f_1} \tag{2.3}$$

The transverse magnification M_t of the display is a complicated expression which is a function of d_0 and the sum $l_2 + l_3$:

$$M_t = \frac{f_1 f_2}{f_1 f_2 + d_0 (f_1 + f_2) - (l_2 + l_3)\ (d_0 + f_1)} \tag{2.4}$$

An analysis of equations (2.2), (2.3), and (2.4) reveals many problems with that general description of synthetic aperture displays:

- According to (2.2) the image will be stable only for a particular value of d_0. Any other value will somewhat smear the image due to motion blur. This is clearly unacceptable for the imaging of deep 3-dimensional objects.
- The display magnification is dependant upon d_0, which creates geometrical distortions in the final image. It is however possible to correct for this effect at the computation step.

2.2.3 Confocal geometry

We will now examine the special case in which $l_2 = f_1$ and $l_3 = f_2$ (confocal geometry). In this degenerate case the conditions for imaging simplify considerably. Equation (2.2) becomes:

$$d_2 = f_1 = \frac{V}{2\omega} \tag{2.5}$$

and equation (2.3) is always satisfied. The transverse magnification of the system then simplifies to:

$$M_t = -\frac{f_2}{f_1} \tag{2.6}$$

and the longitudinal magnification M_l thus becomes:

$$M_l = M_t^2 = \left(\frac{f_2}{f_1}\right)^2 \tag{2.7}$$

The implementation of a practical display is considerably simplified if we adopt a confocal geometry because the match between the linear speed of the fringes on the Bragg cell and the angular rate of the mirror no longer depends on d_0. Deep images can thus be represented without motion

blur. The independence of the system magnification with respect to $d_0$also brings substantial simplifications in the overall design of the display.

The value of f_1 is usually determined from equation (2.5) since v is a constant of the Bragg cell material and ω is constrained by the horizontal scan rate. If we now choose f_2 such that:

$$\frac{f_1}{f_2} = \frac{\Lambda}{\Lambda_f} \tag{2.8}$$

The telescopic magnification of the lens system will be the inverse of the magnification described in section 2.2.1 and the computed object will be displayed with no distortion. For the remainder of this thesis a confocal geometry will be assumed unless stated otherwise.

2.2.4 Display resolution

At any instant in time only a small portion of the image is displayed. From the viewer's perspective the display can be modeled as a narrow aperture being rapidly scanned across a larger hologram (Figure 2.5). It is clear that this narrow aperture, which is also the output pupil, consists of the image of the AOM formed by lenses L_1 and L_2 of Figure 2.4. The maximum useful display resolution is determined by the pupil of the observer. If we assume a diffraction limited system and consider an instant in time in which the diffracted light entirely fills the pupil of the viewer, the maximum resolution condition is given by:

$$\frac{z_1}{S} = \frac{z_2}{s} \tag{2.9}$$

where S is the size of the AOM image and s the diameter of the eye pupil (Figure 2.5). In practice, condition (2.9) cannot be met because the aperture scans across the image and part of the subtend of the eye's pupil will be blocked during a fraction of the scan. The time behavior of the display resolution for a given image location will exhibit the behavior shown in Figure 7. Because the scan time is much smaller than the response time of the eye, the resolution function of Figure 7 is inte-

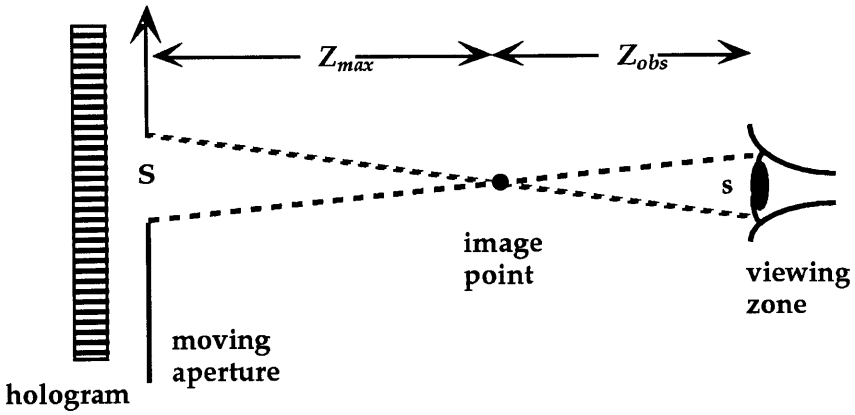

Figure 2.5 Apertured modulator

grated over time by the visual system with the result that the overall resolution will always be inferior to the diffraction limit of the eye, although approaching it asymtotically as S becomes large. In practice, however, a determination of S from (2.9) gives visually excellent results. It is also obvious from (2.9) that the deeper the image, the longer the AOM has to be. The actual size of the AOM can be expressed as:

$$S > \frac{sz_{max}}{M_t(z_{obs} - z_{max})} \tag{2.10}$$

where z_{obs} is the distance between the observer and the AOM image, which is usually close to the output lens, z_{max} corresponds to the section of the image closest to the observer, and M_t is the transverse magnification factor of equation (2.6). As an example, with $M^{-1} = 5$ (corresponding to a view zone having a 14.5 deg. angular width assuming a 50 MHz bandwidth TeO_2 AOM), $z_{max} = 100$ mm, $s = 3$ mm and a viewing distance of 600 mm the minimum required AOM length is 3 mm, corresponding to a space-bandwidth product of 243. Such a figure is well within the range of commercially available TeO_2 AOM's, as some of these exhibit space-bandwidth figures in the thousands[5,6]. For all practical purposes, the display resolution will thus generally be limited by the quality of the system optics or by the algorithms used in the hologram computation.

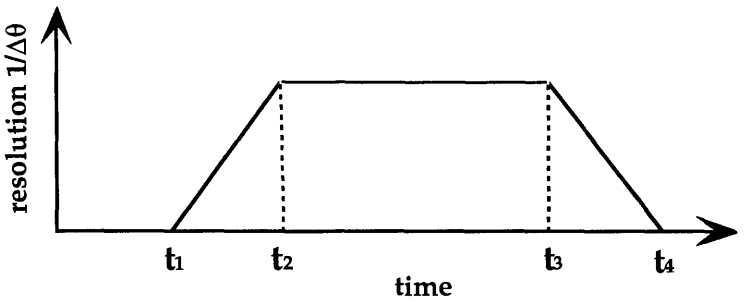

Figure 2.6 Display resolution time dependence for a stationary observer. The diffracted rays are vignetted by the observer's pupil during intervals t_1 - t_2 and t_3 - t_4.

2.2.5 Vertical scanning subsystem

The vertical scanning section of the system is more straightforward because the display exhibits no vertical parallax. The vertical scanning is effected in a raster fashion and its rate (typically from 30 to 60 Hz) places it well within the range of commercially available closed-loop galvanometric scanners[22]. Moreover, the required vertical resolution is relatively low (less than 1000 lines) and remains well within the modulation transfer function limits of ordinary scanning lenses. Because the vertical focal plane is fixed and the horizontal focus is variable, deep images will exhibit some astigmatism, as they do in any horizontal parallax-only autostereoscopic display[14]. This astigmatism can be kept to a minimum if the vertical focal plane coincides with the middle plane of the image. Extensive experience with rainbow holograms shows that this astigmatism remains almost unnoticeable even for fairly deep objects.

A desirable feature of the vertical scanning system is that the output beam be normal to the image plane throughout the field. This condition, known as telecentricity, assures that the displayed image will not become vertically distorted as the horizontal focus is moved away from the vertical focus plane. A telecentric system converts an angular beam deflection to a linear translation by having the scanning element positioned one focal length in front of the output lens[24]. This causes a problem in the confocal system since this space is usually occupied by the horizontal scanning element. The solution is to put the vertical scanner away from the horizontal scanning element and re-image it at the required plane using a cylindrical relay lens L_3 (Figure 2.7). We can then use the

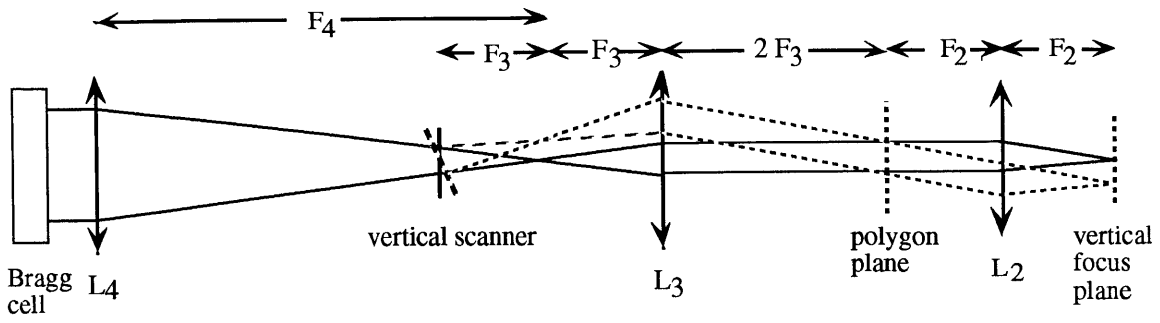

Figure 2.7 Vertical scanning geometry for a single channel Bragg cell. The output lens L_2 is the same as in Figure 2.4. L_3 and L_4 are cylindrical

same lens L_2 both as a horizontal and vertical output lens. The geometry of the vertical scanning subsystem results in a very narrow viewing zone and it is usually necessary to place a one-dimensional diffuser in the vertical focus plane[25]. Such a diffuser can be approximated by a fine pitched lenticular array, or can be produced using holographic techniques[25]. Placing the diffuser in the vertical focus plane of the display increases the view zone by diffusing each line in the vertical direction, but leaves the horizontal image content unaltered.

2.3 Limitations in the original design

2.3.1 AOM space bandwith product

As demonstrated in Chapter I, synthetic holography requires large amounts of information. For example, a hologram having an horizontal size d = 100 mm and an angle of diffraction θ = 30 degrees would require 158 000 samples per scan line for a HeNe laser. Assuming a 50 MHz RF bandwidth (a typical figure for shear mode TeO_2 Bragg cell) and a 60 Hz refresh rate results in a display having less than 11 lines of resolution. This figure is clearly unreasonable for any practical application.

Increasing the number of lines while keeping the refresh rate, view angle and horizontal size constant requires a proportionally larger number of samples per unit time. For a single acoustic channel this translates into a higher operating bandwidth for both the Bragg cell and the associated

electronics. Many factors, however, impose a practical upper bound on the maximum bandwidth. In the case of shear mode TeO_2 this limit comes from the relatively high acoustic attenuation of the material, which is a quadratic function of the operating frequency[5] (this quadratic dependence is a general property of Bragg cell materials). This attenuation limits the useful range of the material to less than 75 MHz if we want to keep a space-bandwidth product larger than 1000. The use of other materials such as Lithium Niobate ($LiNbO_3$) or Gallium Phosphide (GaP) can extend the bandwidth into the gigahertz range, but once again it is very difficult to attain high space-bandwidth products at those frequencies[5,6]. In addition, the electronics associated with the synthesis and signal processing parts of the system become impractical or prohibitively expensive when working at such high bandwidths.

2.3.2 polygonal scanner limitations

The limitations of the polygonal scanning approach become evident if we describe how the design parameters scale with image size and horizontal view zone. I will consider here the case where the horizontal scanning element coincides with the Fourier transform of the Bragg cell phase pattern, i.e., the focal point of lens L_1 of Figure 2.4. At the scanning plane, the size of this Fourier transform is given by:

$$\Delta x = \lambda f_1 \Delta f_s = \lambda f_1 \frac{\Delta \nu}{V} \tag{2.11}$$

where f_1 is the focal length of lens L_1, D f_S is the range of spatial frequencies on the Bragg cell, v is the acoustic velocity of the Bragg cell material and $\Delta\nu$ denotes the frequency range of the signal sent to the transducer.

The frequency range of the signal sent to the Bragg cell is related to the number of samples N and to the horizontal scan period τ by the formula:

$$\Delta \nu = \frac{N}{2\tau} = \frac{d \sin\theta}{\lambda \tau} \tag{2.12}$$

where we have made use of relation (1.3).

It is clear from (2.12) that the size of the Fourier transform, and hence the size of the horizontal scanning element, is proportional to the product of the width and view angle of the desired hologram for a given horizontal scan rate. For a polygonal scanner a number of straightforward calculations lead to the following design parameters[2]:

- The polygon radius R must have a minimum value given by:

$$R \geq \frac{\lambda P^2 \tau \Delta \nu}{2\pi^2} \tag{2.13}$$

where P is the number of polygon facets. Using (2.13) with (2.12) then leads to the result:

$$R \geq \frac{P^2 d \sin\theta}{2\pi^2} \tag{2.14}$$

- The angular speed of the polygon obeys the formula:

$$\omega = \frac{2\pi}{P\tau} \tag{2.15}$$

A few numerical explorations easily demonstrate that using a polygon as the horizontal scanning element becomes impractical for images more than a few centimeters across. As an example, an image with a horizontal size of 20 cm and a view angle of 20 degree would require a polygon having a radius of 50 cm, assuming a 12-sided element spinning at 12 000 rpm.

III HOLOGRAM PLANE SEGMENTATION

3.1 Divide and Conquer

I described in section 2.3.1 how the space bandwidth product limitations of both Bragg cells and digital electronics severely restrain the attainable image size. A solution to this problem may consist of dividing the holographic image into a large number of subelements, with each of these elements having only to process a small fraction of the total optical and computational load. This approach has paid off in the computer science field, where massively parallel computers designed by Thinking Machines Corp, Maspar Inc., and Intel have proven the validity of the "divide and conquer" principle. The use of parallelism is also actively investigated in the optical signal processing community. Indeed, one of the principal motivations behind the development of optical processors lies in their inherent capability for parallel operation.

The next task is now to determine the most efficient way to divide the imaging system into a subset of parallel operations. An obvious candidate is the line scanning operation since the horizontal scan lines are essentially independent from each other. This is a consequence of the horizontal parallax only nature of the display. Simultaneously writing N horizontal scan lines at a time divides the bandwidth required by each individual acoustic channel by a factor N. In theory large holograms could be written with relatively low bandwidth electronics if N is sufficiently large.

3.2 Multiple channel Bragg cells

3.2.1 Description

It could be feasible to use N different Bragg cells and then combine their output by optical means but such an approach would be expensive and bulky. In addition, optically registering the N different horizontal lines would likely be quite difficult to achieve. Fortunately for the author of this

thesis it has proved feasible to simultaneously address a large number of acoustic channels on the same acousto-optic substrate. Multichannel Bragg cells have been investigated in the optical signal processing community since the 1960's and cells with as many as 128 channels have been described[41].

A simplified drawing of a multichannel Bragg cell is shown in Figure 3.1. A piezoelectric transducer is mechanically bonded with metallic thin films to the acousto-optic material. The metallic bonding layer also serves as the bottom electrode for the transducer assembly. The top electrode layer contains multiple electrodes and each electrode defines a single channel of the device.

The design of an individual channel of a multichannel Bragg cell is smilar to that of a single channel device. Multiple electrodes on a single substrate, however, impose additional design constraints[42]. These include the minimization of electrode spacing, adjacent channel crosstalk, and consideration of thermal constraints.

3.2.2 Multichannel Bragg cell design considerations

In this section I will describe the different constraints on multichannel deflectors and describe the necessary tradeoffs in the implementation of such devices and I will loosely follow the development of refs. 7 and 42. I will first discuss the case of isotropic materials and extend it to anisotrpoic materials in the next section.

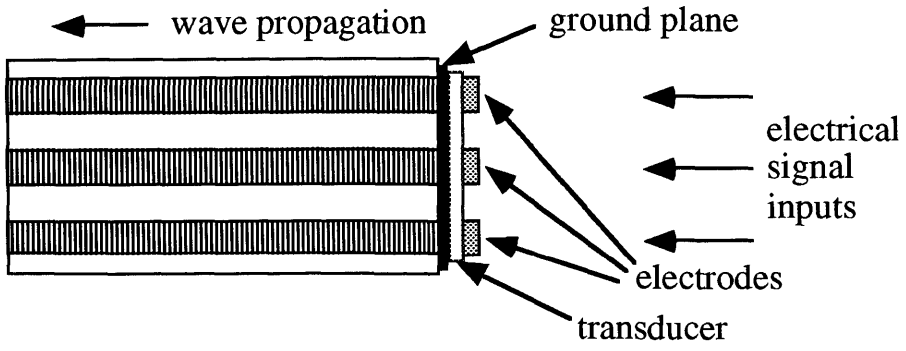

Figure 3.1 Typical multichannel Bragg cell configuration

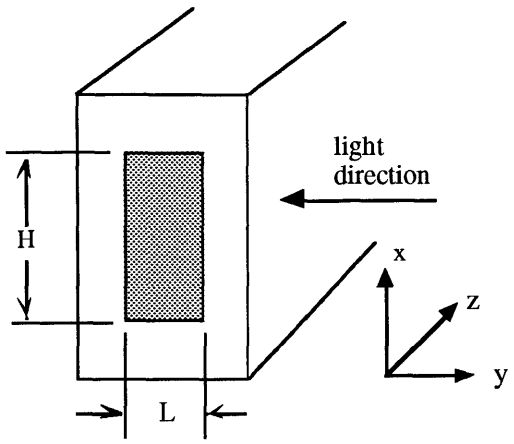

Figure 3.2 Geometry for integrated optical effects calculations.

The ideal diffraction efficiency of an AOM with a transducer of length L and height H (Figure 3.2) is:

$$\eta = \frac{I_{diffracted}}{I_{incident}} = \sin^2\left[\frac{\pi}{\lambda\sqrt{2}}\left(M_2 P \frac{L}{H}\right)^{\frac{1}{2}}\right] \tag{3.1}$$

where P is the input power and M_2 is a figure of merit specific to each acousto-optic material. This figure of merit is often used when comparing materials since it determines how much power is necesssary to attain a given diffraction efficiency. M_2 is expressed as:

$$M_2 = \frac{n^6 p^2}{\rho V^3} \tag{3.2}$$

where n is the index of refraction, p is the photoelastic coefficient, and ρ is the density of the material. The values of M_2 for a few commonly used materials are given in Table 3.1. Longitudinal mode TeO_2 clearlystands out as an exceptional material in this respect.

In the holographic video display the efficiency is kept low so that it varies nearly linearly with the power of the input electric signal.

It is important to determine the shape of the acoustic field when using multiple channel since the acoustic leakage from one channel to another is the prime source of interchannel crosstalk. The sound field radiated from the transducer diffracts in a fashion similar to the spreading of a light field so that the sound field can be calculated using the Huygens-Fresnel diffraction formula[43]. For an isotropic material the far field pattern is thus related to the Fourier transform of the aperture shape. For example, the far field pattern $E(\theta)$ of a square transducer is, in the y-direction:

$$E(\theta) = K\left\{\frac{\sin\left(\frac{H\theta}{\Lambda}\right)}{\frac{H\theta}{\Lambda}}\right\}^2 \tag{3.3}$$

where θ is the angular direction from the normal to the transducer plane and K is a constant. In the near field the acoustic field profile is given by a Fresnel integral. For a square transducer the expression is:

$$E(x, z) = \frac{\exp(-ikz)}{\sqrt{-i\Lambda z}}\int_{-\frac{H}{2}}^{H/2} \exp\left[\frac{i\pi}{\Lambda z}(x - x_0)^2\right]dx_0 \tag{3.4}$$

The near field of the acoustic field extends into the material at a distance D. The distance D is defined as the point where the first null in the acoustic energy pattern intercepts the projection of the transducer edge. The transducer height is chosen so that D coincides with the time-aperture distance of the Bragg cell. For a rectangular electrode this distance is:

$$D = \frac{H^2}{\Lambda} \tag{3.5}$$

The separation of the channels in a multichannel device is chosen as to minimize the acoustic crosstalk while keeping the fill factor as high as possible to make an efficient use of the material. This acoustic crosstalk arises from the presence of acoustic sidelobes in the near field pattern as described by (3.4). The sidelobes can be minimized by electrode apodization. Good results have also been obtained by using diamond or trapezoid shaped electrodes[7]. The crosstalk factor

between two acoustic fields generated by rectangular electrodes at the distance z has been calculated in reference[7] and is described by the expression:

$$C_t = \frac{\Lambda z}{2\pi^2 S^2} \frac{1 + (H^2/4S^2)}{[1 - (H^2/4S^2)]^2} \tag{3.6}$$

where S is the center to center spacing between electrodes. At the distance D defined in (3.4) the crosstalk becomes:

$$C_t = \frac{H^2}{2\pi^2 S^2} \frac{1 + (H^2/4S^2)}{[1 - (H^2/4S^2)]^2} \tag{3.7}$$

To hold the isolation to greater than 20 db over the length D the aperture to spacing ratio must be less than one third.

For multichannel operation it is desirable to operate at high acoustic frequencies in order to minimize the crosstalk and thus be able to stack a larger number of channels on the same substrate. The acoustic attenuation, which varies as the square of the frequency, imposes an upper limit on the operating frequency for a given space bandwidth product.

Equations (3.3) to (3.7) are valid in the case of rectangular electrodes. Both the acoustic spreading and crosstalk values can be reduced by the use of apodized or diamond shaped electrodes[7]. By generating an acoustic profile which approximates a Gaussian distribution the diffraction of the acoustic field is reduced in a fashion similar to the case of a Gaussian laser beam (which is to be expected since the distribution of both fields is described by the Huygens-Fresnel formula). Most commercially available multichannel devices now use apodized electrodes.

3.2.3 The anisotropic case

Equations (3.3) to (3.7) describe the case of an isotropic material such as fused quartz or certain types of flint glasses. Most acousto optic materials are crystalline in nature, however, and thus

exhibit anisotropic properties. In an anisotropic crystal the phase velocity of the acoustic waves varies as a function of the direction of propagation relative to the orientation of the crystal. The effect of acoustic anisotropy have been studied extensively in refs. 43 and 44 and will be summarized here.

The acoustic anisotropy of a material is characterised by the material acoustic anisitropy b. b is zero in the isotropic case. In anisotropic materials the power flow direction is different from the propagation direction. It can be proved that the effect of anisotropy on the propagation of a sound field close to the principal axes of the crystal is to multiply the acoustic wavelength Λ by the factor $(1\text{-}2b)$ to obtain an effective wavelength $\Lambda(1\text{-}2b)$. When b is negative the material exhibits larger acoustic spreading than the isotropic case. When $b > 0$ the acoustic waves diverge more slowly than in isotropic materials. Some materials have self-collimating modes where b is close to 0.5. In those materials the beam divergence essentially vanishes, a property that renders them very attractive for multichannel Bragg cells.

The values of b for some commonly used acousto-optic materials are given in Table 3.1.

material	orientation	mode	M_2	velocity (km/s)	attenuation (dB/μs-GHz^2)	b
GaP	[1-10]	shear		4.13	1.5	0.487
TeO_2	[001]	longitudinal	34.5	4.2	15	0.24
TeO_2	[110]	shear	793	0.617	220	-26
$PbMoO_4$	[001]	longitudinal	36.3	3.63	15	-0.18
$LiNbO_3$	[100]	longitudinal	7.0	6.57	0.15	
$LiNbO_3$	[001]	shear	2.92	3.59	2.6	

Table 3.1 Properties of selected acousto-optic materials

We can see from Table 3.1 that the values of b vary considerably between different materials. The [1-10] propagation mode of gallium phosphide is almost perfectly collimated, a fact that makes this material very attractive for signal processing applications. Unfortunately a number of other factors seriously limit the usefulness of this material for our application, the principal one being

that the material is only transparent in the red part of the spectrum. These limitations will be explained in the following section.

Longitudinal mode TeO_2 exhibits some degree of self-collimation, while shear mode TeO_2 shows a very large amount of acoustic spreading. One could think that this large spreading factor precludes the use of shear mode tellurium dioxide for multichannel devices, but its extraordinary figure of merit M_2 stil makes it a leading contender for low bandwidth systems.

3.2.4 Selection of suitable materials

The selection of a suitable acoustic material for use in a multichannel Bragg cell depends on a number of parameters and is a complex design decision. The figure of merit M_2 and the spreading factor b have already been described. Among the other main factors to be considered are

- *Acoustic attenuation of the material.* This parameter varies with the square of the frequency and thus places a limit of the maximum bandwidth that can be acheived for a given cell size. The high acoustic attenuation of shear mode TeO_2 limits its operation to below 100 MHz in most cases.
- *Optical transmission.* The material has to be transparent across the specified wavelengths. In the case of an electronic holography display the material should be highly transmissive across the visible spectrum. This limits the use of gallium phosphide, which is transmisssive only in the red part of the spectrum.
- *Thermal conductivity.* A large number of closely spaced transducers inject significant amounts of acoustic energy in a material. This energy eventually gets dissipated as heat. The resulting thermal gradients can cause acoustic velocity and spatial refractive index gradients that can interfere with the proper operation of a Bragg cell if the thermal conductivity of the material is not sufficient.
- *Good mechanical and chemical properties*. The material has to be non-hygroscopic and no extraordinary procedures should be necessary to cut and polish it.

- *Commercial availability.* It should be possible to grow high quality boules of a sufficient size at a reasonable cost.

The materials most commonly described in the litterature for multichannel operation are longitudinal mode TeO_2, shear mode GaP, and lithium niobate. Devices based on those materials are commercially available from vendors such as NEOS Corp. , Brimrose Corp., Crystal Technology, and Isomet Corp. In the system design section (Chapter III) I will give an example of the selection process and design of a multichannel Bragg cell.

3.3 Vertical scanning subsystem

The horizontal scanning requirements for a multichannel system are the same as for a single channel. Multichannel operation places several constraints on the vertical scanning subsystem, however. Figure 3.3 describes a typical optical configuration for a multichannel holographic video display.

The vertical scanning subsystem has to perform the following functions:

- project a real image of the Bragg cell on the output plane of the display with a correct magnification factor
- vertically scan that real image so that the combination of horizontal and vertical scanning creates a seamless raster.

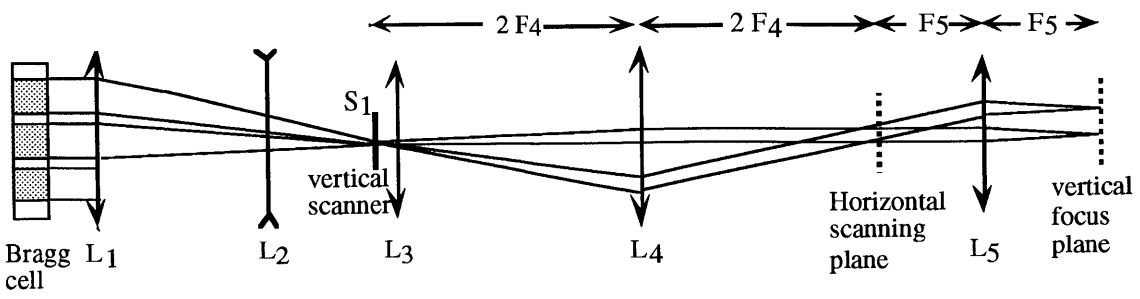

Figure 3.3 Vertical axis scan optics for a multichannel system.

Two additional constraints are also made necessary by the requirement that the horizontal and vertical scanning mirrors be as small as possible such that their inertia is minimized. Mirror inertia is an important factor in galvanometric scanner systems since a low inertia allows for faster and more precise beam positioning.

The vertically collimated light diffracted by the Bragg cell is focused down on the vertical scanning mirror S_1 by the combination of lenses L_1 and L_2. L_4 images the plane defined by S_1 on the horizontal scanning element S_2 so that both the horizontal and vertical scanning planes coincide with the front focal plane of L_5. This assures that the scanning system is telecentric in both the horizontal and vertical directions. L_3 is placed as close to the S_1 plane as possible and is chosen so that the Bragg cell is imaged at the correct position in the output plane. In most cases it is desirable to have the Bragg cell imaged at the same plane by both the horizontal and vertical scanning optics to minimize the amount of astigmatism.

The combination of lenses L_1, L_2, L_3, and L_5 determines the vertical magnification of the Bragg cell in the image plane. In most implementations of the display L_1 and L_5 are spherical lenses shared by the horizontal and vertical imaging subsystems. This leaves L_2 and L_3 as free parameters to determine the vertical magnification and imaging plane. The optical configuration described above has the advantage that it allows for a wide latittude in the choice of the Bragg cell's channel spacing. This in turns renders it possible to optimize the multichannel Bragg cell parameters independently of the display optics.

IV FOURIER PLANE SEGMENTATION

4.1 Replacing the polygon by a galvanometric scanner.

4.1.1 Motivation

As I have demonstrated in section 2.3.2 it rapidly becomes impractical to use a polygonal scanner as we scale up the display. The fundamental reason is that the size of the Fourier transform of the image is proportional to the product of the size and view zone of the hologram. Combining equations (2.5) and (2.10) yields the result:

$$\Delta x = \frac{\lambda \Delta \nu}{2\omega} \tag{4.1}$$

where $\Delta\nu$ is the radio-frequency bandwidth of the signal sent to the Bragg cell and ω is the angular frequency of the Fourier plane scanning element. Combining (4.1) with (2.12) then gives us:

$$\Delta x = \frac{d \sin\theta}{2\omega\tau} \tag{4.2}$$

where τ is the active period of a scan line. We can rewrite (4.2) in the form

$$\Delta x = \frac{d \sin\theta}{2\Omega} \tag{4.3}$$

with Ω being the total angular excursion corresponding to a scan line. Thus the only way to reduce the size of the Fourier transform is to augment Ω. The f/number of the output lens scales linearly with the scan angle, so in practice Ω is generally kept below 15 degrees (equivalent to a 30 degrees optical deflection range).

In a polygonal mirror each facet has to exceed the Fourier transform size, a situation that rapidly leads to impractical figures. A possible solution to this problem is to use a galvanometric scanner as the horizontal scanning element. Since we require a constant angular velocity scanning over the entire deflection range, the galvanometric scanner is fed with a triangle or sawtooth waveform. For an horizontal scanner the size of the scanning mirror is simply given by the extent of the Fourier transform (4.3).

4.1.2 Scan frequency

The advantage of the galvanometric scanner approach is that the mirror size (and thus the size of the scanning section) is always much smaller than the diameter of a corresponding polygonal scanner. The main drawback comes from the lower scanning speed achievable with galvanometric scanners. The angular speed of galvanometric scanners rapidly decreases with mirror inertia (and thus size), but the requirement of an acceptable display refresh rate constrains the scan rate to aminimum value. The scanning period τ_{scan} is related to the display parameters by the relation:

$$\tau_{scan} = \tau + \tau_r = \frac{d \sin\theta}{\lambda \Delta\nu} + \tau_r \tag{4.4}$$

where τ_r corresponds to a retrace interval made necessary by the mirror inertia. The display refresh rate f_u is then:

$$f_u = \frac{M}{N \tau_{scan}} \tag{4.5}$$

where M is the number of acoustic channels in the Bragg cell and N is the total number of horizontal lines in the display.

A simple numerical example is useful to illustrate the problems encountered if we use a single mirror as our Fourier transform scanning element. We assume an image with the characteristics defined in Section 2.3.1 (θ = 30 deg., d = 100 mm, $\Delta\nu$ = 50 MHz) and an optical deflection in the

Fourier plane of 30 degrees. Applying equation (4.3) results in a Fourier transform (and mirror) size of 95 mm. The minimum scan period is then 1.58 msec., corresponding to a scanner frequency of 633 Hz if no retrace interval is present. No commercially available technology, however, can satisfy these requirements.

A lower scan rate can be acheived if we add a substantial retrace time or diminish the bandwidth of the electrical signal, but this comes at the expense of the number of holographic lines if we keep the refresh rate constant. Although a retrace time is inevitable in any electromechanical system, we want the active duty cycle to be as high as possible. Likewise, we want to make full use of the bandwidth attainable by the display electronics.

4.2 Segmenting the Fourier plane

It is clear from the previous section that there are quite serious limitations in using a single galvanometric deflector as the Fourier transform scanning element. However, at any given moment the pupil of an observer will intersect only a small part of the diffracted light, as Figure 4.1 demonstrates. A reasoning based on spatial frequency concepts clearly illustrates this. The pupil of the observer subtends only a small fraction of the total spatial frequency spectrum in the image plane. This spectral range corresponds to a small spatial extent in the Fourier plane.

We can thus conclude that no difference in the image content would be noticeable if only that small portion of the front focal plane that subtends the pupil would be scanned (provided, of course, that the observer does not move). This suggests that under the proper conditions the large scanning element at the Fourier plane could be replaced by an array of smaller mirrors without significant image degradation. the determination of those conditions, as well as the exact impact of mirror segmentation on the image characteristics, will be the focus of this chapter.

4.3 Geometrical interpretation

The most intuitive way to analyze the consequences of the Fourier plane segmentation is to use a geometrical approach. To this end, we model the last section of the holographic display as a lens which images the scene of interest at a variable conjugate ratio. We also consider that the image of the AOM always satisfies the condition (2.9) so that we can ignore its existence in this analysis. In this static model the scanning mirror defines the pupil of the imaging system. An analysis which takes into account the effects of the Bragg cell characteristics will be presented in the next section.

The human visual system will not notice a decrease in image quality if the spot size of the light deflected by any single scanner is smaller than the resolving power of the eye. This can be stated in geometrical terms by requiring that the exit pupil of an image projected by each scanner be larger than the pupil of the eye:

$$l_{mirror} \geq \frac{P^{eye} f_2}{D_{view}} \tag{4.6}$$

where P^{eye} denotes the human pupil size (typically about 3 mm), f_2 is the focal length of the output imaging lens, and D_{view} denotes the viewing distance. It is to be noted that relation (4.6) is independent of the separation between the output lens and the image. This property derives from the fact that the aperture stop is situated in the front focal plane of the imaging lens. All the principal rays in the image space are thus parallel to the optical axis of the lens. Such a system is said

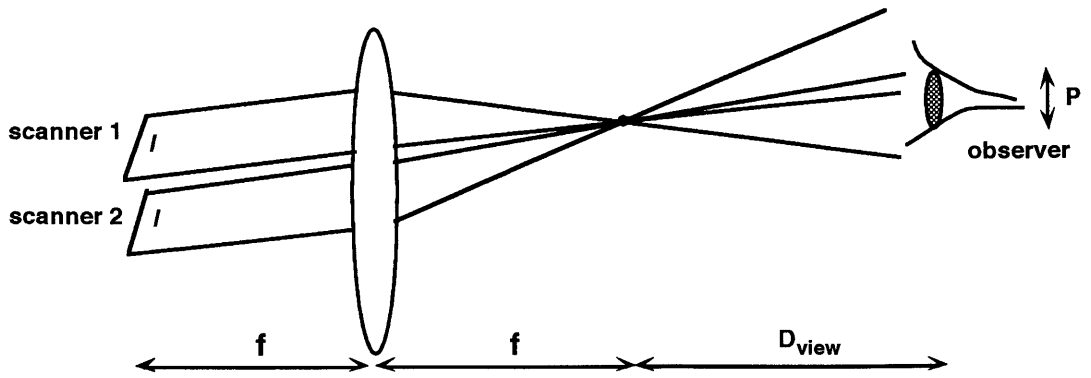

Figure 4.1 Multiple scanner geometry

to be *telecentric on the image side.* The interested reader will find a demonstration of (4.6) in Appendix B.

There is necessarily a gap between each deflecting mirror. This gap will be projected as a dark area at the viewer plane. The pupil of the observer intersecting the interscanner gap has two consequences:

- There is a decrease in the total intensity reaching the observer's retina
- The perceived resolution of the scene is diminished because the effective system pupil is reduced.

It is thus essential that the gap between each scanner be small compared to the eye pupil (Figure 4.1) so that fluctuations in light intensity as the observer moves sideways remain acceptable. That condition can be stated as:

$$l_{gap} \ll \frac{P^{eye} f_2}{D_{view}} \tag{4.7}$$

In addition to the intrinsic gap l_{clear} due to the mirror clearance at rest an additional component is introduced when the mirrors are rotated (Figure 4.2). The total spacing between the mirrors can thus be deduced from a simple trigonometric calculation:

$$l_{gap} = l_{clear} + l_{mirror}\left[1 - \cos\left(\frac{\theta}{2}\right)\right] \tag{4.8}$$

where θ is the total mechanical scan excursion.

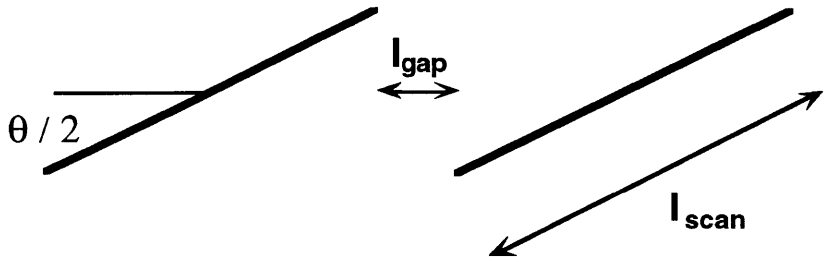

Figure 4.2 Interscanner gap

Equations (4.6) to (4.8) show that the mirror size has to be within a certain range for the image to be acceptable. Mirrors which are too small will reduce the resolution of the display while excessive dimensions lead to noticeable gaps.

4.4 Spatial frequency analysis

4.4.1 Introduction

The previous ray tracing model is very useful in the determination of the general geometrical requirements of the display. However, it does not provide a quantitative description of image resolution with respect to such factors as scanning mirrors size, Bragg cell frequency response, and wavelength. In the realm of optics, such questions are usually answered by using a spatial frequency analysis. In this section I will proceed to such an analysis in the case of coherent and incoherent Bragg cell illumination.

Coherent illumination by the means of a laser has historically been the preferred type of illumination for electronic holograms[1,2,25,49,48] for the reason that laser light is easy to manipulate, and that coherent sytems are usually simpler to analyze[51]. The disadvantage of coherent illumination stems from the difficulty in avoiding coherent noise (speckle) in the image. Laser light sources of sufficient power for large size displays are also quite expensive.

Partially coherent light sources solve the speckle problem, and might eventually prove less expensive than lasers. Candidates for such light sources include superluminescent Light Emitting Diodes (LED's) and arc lamps. It might also prove possible to use gain guided visible laser diodes whose mode structure has been scrambled over time by varying their drive current as partially coherent sources. The analysis of incoherent systems, which is based on partial coherence theory, is however somewhat more complicated.

4.4.2 Coherent illumination

4.4.2.1 *Intermirror coherence*

When analysing the behavior of a multiple mirror system it is essential to determine the effects of phase coherence between mirrors. Optical systems which incorporate multiple actuated mirrors are becoming increasingly useful in optical astronomy since they remove the mechanical constraints that limit the size of single mirors and can be used to compensate for atmospheric aberrations. In those systems the phase relation between each reflecting surface has to be kept rigorously (less than 1/10 wave) constant to maintain the resolving power of the telescope.

The MIT holographic video display, however, does not require a phase match between mirrors as long as each mirror obeys condition (4.6). Indeed, such a phase match would be impossible to maintain during scanning, as the following reasoning will demonstrate.

Let us suppose that the successive mirror edges of Figure 4.1 have a phase difference φ at the beginning of the scan. As the mirrors rotate during a scan the distance between the mirror edges will vary, and thus the phase difference between edges will change at the rate:

$$\frac{d\varphi}{dt} = \frac{4\pi\omega l}{\lambda} \tag{4.9}$$

As an example, a 1 cm wide mirror will see the phase of its edge change by 52 000 radians with respect to its neighbors during a single 15 deg. scan. The excursion time corresponding to a single scan will always be considerably smaller than the integration time of the human eye (a condition made necessary by the need to avoid flicker), with the consequence that the mirrors can be considered as being completely incoherent from each other.

The mutual incoherence of adjacent mirrors signifies that no interference effects between mirrors, which could result as intensity variations in the image plane, will be observable. It thus acts in the advantage of the observer, a situation opposite to the case of astronomical optics.

4.4.2.2 *Spatial frequency response*

In the remainder of this chapter I shall consider the holographic video display as a diffraction limited optical system. This assumption is reasonably close to reality if we consider the optics between the laser and the horizontal scanning mirrors since in practice most components in that section operate at relatively high f/numbers. Most of the aberrations in the display come from the output lens whose aperture is very large (with f/numbers typically between 1.2 and 2).

The spatial frequency response of the display is simply the product of the spatial frequency response of the Bragg cell/signal processing electronics times the magnification factor M:

$$\Delta f_x = \frac{M\Delta v}{V} = \frac{f_2}{f_1}\frac{\Delta v}{V} \tag{4.10}$$

Equation (4.10) assumes that the mirror array covers the entire Fourier spectrum and that the output lens is large enough to avoid vignetting. These conditions are usually met in practice.

4.4.2.3 *Impulse response and coherent transfer function*

In an imaging system we can consider the image as a convolution of the image predicted by geometrical optics with an impulse response that is determined by the exit pupil of the system[51]. The image amplitude can be written as

$$U_i(x_i) = \int_{-\infty}^{\infty} h(x_i - x_o)\, U_g(x_o)\, dx_o \tag{4.11}$$

where U_g is the ideal image predicted by geometrical optics and h is the impulse response of the imaging system. h is simply the Fraunhofer diffraction pattern of the exit pupil:

$$h = K\int_{-\infty}^{\infty} P(x) \exp\left(-i\frac{2\pi}{\lambda d_i}\right) dx \tag{4.12}$$

where K is a constant.

The coherent transfer function $H(f_x)$is defined the Fourier transform of the inpulse response and is thus described as:

$$H(f_x) = P(\lambda d_i f_x) \tag{4.13}$$

The problem of determining the display resolution in the image plane is thus reduced to the determination of the smallest pupil in the system. If we exclude the pupil of the observer and consider each lens in the system to be of adequate size we can distinguish three pupils:

- The RF spectrum pupil.
- The Bragg cell pupil.
- The scanning system pupil.

The signal processing electronics temporal frequency response defines an effective pupil that is determined by the maximum and minimum values of the RF spectrum sent to the transducers. The geometrical interpretation of this effect is easy to understand if we consider a single point imaged by the Bragg cell (Figure 4.3). The physical size of the pupil at the Bragg cell plane is then given by the formula:

$$P_o^{\Delta\nu} = \frac{2\lambda d_o \Delta\nu}{v} \tag{4.14}$$

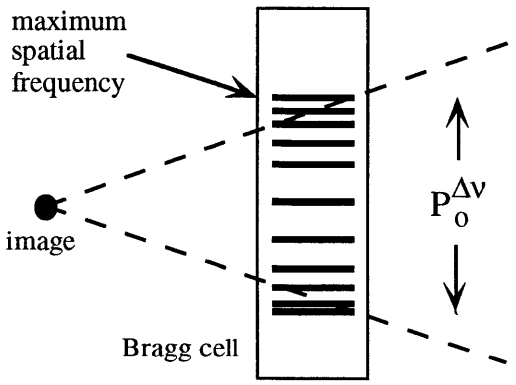

Figure 4.3 The spatial frequency range on the Bragg cell defines an effective aperture $P_o^{\Delta\nu}$

where d_o is the distance between the Bragg cell and the image (or equivalently, the focal length of the Fresnel lens written on the Bragg cell).

It is more convenient to work in the image space where the image of the Bragg cell has been demagnified by the confocal system described in section 2.2.3. In that space the Bragg cell is imaged close to the focal plane of the output lens. If we follow the prescriptions of section 2.2.3, the distance d_i between the image of the Bragg cell and the image of our original point will match the calculated value. In the space imaged by the output lens the laws of geometrical optics give the relations

$$d_i = M^2 d_o \tag{4.15}$$

$$P_i^{\Delta\nu} = M P_o^{\Delta\nu} \tag{4.16}$$

where $M = f_2/f_1$ is the transverse magnification ratio. Combining (4.14), (4.15), and (4.16) result in the expression

$$P_i^{\Delta\nu} = \frac{2\lambda d_i \Delta\nu}{MV} \tag{4.17}$$

The size of the RF pupil is of course bound by the physical extent of the Bragg cell P_o^{cell}. In the image space we have thus the relation:

$$P_i^{\Delta\nu} \leq P_i^{cell} \tag{4.18}$$

where $P_i^{cell} = M P_o^{cell}$ is the horizontal extent of the Bragg cell image. The coherent transfer function of the Bragg cell / signal processing subsystem (assuming no other pupils are present in the display) can thus be described as:

$$H(f_x) = \text{rect}\left(\frac{\lambda d_i f_x}{\min\left[P_i^{\Delta v}, P_i^{cell}\right]}\right) = \text{rect}\left(f_x \max\left[\frac{Mv}{2\Delta v}, \frac{\lambda|d_i|}{MP_o^{cell}}\right]\right) \tag{4.19}$$

where the rectangle function is defined as

$$\text{rect}(x) = \begin{cases} 1 & |x| \le 1/2 \\ 0 & otherwise \end{cases} \tag{4.20}$$

The mirror array constitutes the third pupil in the display. The sections of spatial frequency spectrum scanned by adjacent mirrors can be considered as incoherent to each other, with the consequence that their contributions to the image sum incoherently. The consequence of this incoherent summing is that the impulse response of the scanning array is limited by the spatial extent of each single mirror. Thus when computing the coherent transfer function the horizontal extent of a single mirror constitutes the effective pupil:

$$P_{scan} = l \tag{4.21}$$

Since the mirror pupil is situated at the Fourier plane of the imaging lens the coherent transfer function of the display is given by

$$H(f_x) = \text{rect}\left(\frac{\lambda f_2 f_x}{l}\right) \tag{4.22}$$

Equations (4.19) and (4.22) can be combined to yield the overall coherent transfer function H^{system}:

$$H^{system}(f_x) = \text{rect}\left(f_x \max\left[\frac{\lambda f_2}{l}, \frac{Mv}{2\Delta v}, \frac{\lambda|d_i|}{MP_o^{cell}}\right]\right) \tag{4.23}$$

The modulus of the system point spread function is then calculated to be:

$$|h|^2 = \begin{cases} \dfrac{l^2}{\lambda^2 f_2^{\,2}} \operatorname{sinc}^2\left(\dfrac{l x_i}{\lambda f_2}\right) & \dfrac{l}{f} \le \dfrac{\min\left[P_i^{\Delta v}, P_i^{cell}\right]}{d_i} \\ \dfrac{\left(\min\left[P_i^{\Delta v}, P_i^{cell}\right]\right)^2}{\lambda^2 d_i^{\,2}} \operatorname{sinc}^2\left(\dfrac{x_i \min\left[P_i^{\Delta v}, P_i^{cell}\right]}{\lambda d_i}\right) & otherwise \end{cases} \tag{4.24}$$

4.4.3 Incoherent illumination

I explained in section 4.4.1 that it might prove advantageous to use incoherent light sources for electronic holography displays, their principal advantage being that they considerably reduce speckle noise. To analyze the spatial frequency response of systems using incoherent sources it becomes necessary to use an analysis based on incoherent imaging. An excellent treatment of incoherent imaging concepts can be found in reference 51, upon which is based the analysis of this section. Because the MIT electronic holography display exhibits horizontal parallax only, a one-dimensional analysis will be applied here.

Incoherent imaging systems obey the intensity convolution integral and are frequency-analyzed as linear mappings of intensity distributions. Designating the spatial frequencies along the x-axis as f_X, it can be shown[51] that the incoherent transfer function $H'(f_X)$ is related to the coherent transfer function $H(f_X)$ by the formula:

$$H'(f_x) = \frac{\int_{-\infty}^{\infty} H\left(\xi - \frac{f_x}{2}\right) H^*\left(\xi + \frac{f_x}{2}\right) d\xi}{\int_{-\infty}^{\infty} |H(\xi)|^2 d\xi} \tag{4.25}$$

The function H is usually referred to as the optical transfer function(OTF) of the system and its modulus is known as the modulation transfer function (MTF). In an optical system without aberrations the OTF is calculated using the pupil function $P(\lambda d_i f_X)$ as the coherent transfer function(d_i being the pupil to image distance). For a system with aberrations, the same reasoning can be

applied provided we use the generalized pupil function P′ as the coherent transfer function[51]. P′ can be written as:

$$P'(\lambda d_i f_x) = P(\lambda d_i f_x) \exp[jkW(\lambda d_i f_x)] \tag{4.26}$$

where the product $kW(x)$ represents the phase error resulting from the system aberrations at the point x. The calculation of the incoherent OTF is thus reduced to the determination of the phase error followed by the application of (4.26) with P' in lieu of H. Since in this analysis I consider the display to be diffraction-limited, I will assume the pupil function to be real and determined by the coherent pupil function described in eq. (4.13).

The pupils described in section 4.4.2.2 are all real and have edges described by step functions. For imaging systems incorporating such pupils the OTF is quite easy to calculate and id described in ref. 51. For rectangular pupils the OTF is related to the coherent cutoff limit f_0 by the relation:

$$H'(f_x) = \Lambda\left(\frac{f_x}{2f_0}\right) \tag{4.27}$$

where Λ is the triangle function defined as

$$\Lambda(x) = \begin{cases} 1-|x| & |x| \le 1 \\ 0 & otherwise \end{cases} \tag{4.28}$$

Since the coherent cutoff frequency f_0 for the display has been determined in the previous section the determination of the incoherent transfer function is straightforward. Using (4.27) with (4.23) directly gives the result:

$$H'(f_x) = \Lambda\left(f_x \max\left[\frac{\lambda f_2}{l}, \frac{Mv}{2\Delta v}, \frac{\lambda|d_i|}{MP_o^{cell}}\right]\right) \tag{4.29}$$

4.4.4 Effect of the observer's pupil

The results determined in sections 4.4.2 and 4.4.3 correspond to the spatial frequencies observed is a piece of photographic film were placed at the image focus. The final image is created on the observer's retina by the eye lens. A complete description of the display should take into account the effect of the human eye, which will be modeled as a diffraction limited lens with a focal length f^{eye} and a pupil function P^{eye}.

As explained in section 4.3, the perception of the holographic image is optimum when the eye does not straddle the projection of an intermirror gap. This condition obviously cannot be met in cases where the projection of the mirror aperture is smaller than the eye pupil. In that case, the resolution is limited by the aperture of a single mirror because the contibutions from each mirror are incoherently summed. The best possible image OTF is found by modifying equation (4.29) to take the imaging characteristics of the eye into account. The OTF at the plane of the eye retina is thus written as:

$$\mathrm{H}\left(f_x^{\,eye} \right) = \Lambda\left(f_x \max\left[\frac{\lambda d_i^{\,eye}}{P^{eye}}, \frac{d_i^{\,eye}}{z_{obs}} \frac{\lambda f_2}{l}, \frac{d_i^{\,eye}}{z_{obs}} \frac{Mv}{2\Delta\nu}, \frac{d_i^{\,eye}}{z_{obs}} \frac{\lambda |d_i|}{MP_o^{\,cell}} \right] \right) \tag{4.30}$$

where $d_i^{\,eye}$ is the distance between the eye lens and the image on the retina and z_{obs} is the distance between the observer and the plane of the hologram.

Equation (4.30) gives the OTF of the holographic image on the retina of the observer's eye. For most practical purposes, however, we are more interested in the spatial frequencies of the image on the plane of the hologram. These are related to the retinal spatial frequencies by the magnification of the eye lens:

$$\mathrm{H}\left(f_x^{\,i} \right) = \mathrm{H}\left(\frac{z_{obs}}{d_i^{\,eye}} f_x^{\,eye} \right) = \Lambda\left(f_x \max\left[\frac{\lambda z_{obs}}{P^{eye}}, \frac{\lambda f_2}{l}, \frac{Mv}{2\Delta\nu}, \frac{\lambda |d_i|}{MP_o^{\,cell}} \right] \right) \tag{4.31}$$

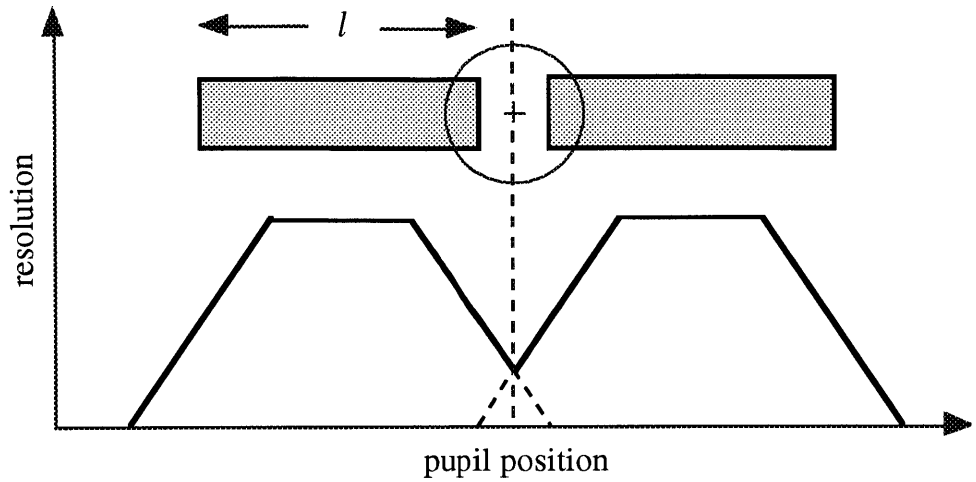

Figure 4.4 Variation in display resolution as the eye pupil moves across the intermirror gap. The resolution is minimum when the pupil straddles the gap.

equations (4.30) and (4.31) are valid if either one of two conditions is fulfilled:

- The eye of the observer is colinear with the projection of a mirror image or
- The scanning mirror size is much smaller than the eye pupil so that at least one complete mirror image occupies the eye pupil for any observer position.

Those conditions are not met when the eye straddles the boundary between two mirrors. In that case the resolution will decrease as the eye moves across to attain a minimum when the eye pupil is centered on the gap between successive mirrors. Figure 4.4 describes how the resolution varies as the eye moves across the intermirror gap.

4.5 Discussion

As the above discussion makes clear there is an optimum mirror size which will result in a maximum overall resolution while keeping the effect of the gaps to a minimum. This condition is met when we have an equality in equation (4.6). In practice this condition imposes an optimum mirror size in the order of a millimeter. No commercially available galvanometric scanner technology can allow such a tight packing of scanning elements, however, and thus in practice the mirror size will be limited by the physical size of the galvanometric element. An optimal mirror array could pos-

sibly be manufactured with the silicon micromachining technologies being developed in a number of laboratories. This opens the door to large, solid state displays almost within reach of today's technology.

Bragg cells having a large aperture and corresponding high space bandwidth product value are commercially available in many materials. Thus in practice the Bragg cell aperture P^{cell} is not a limiting factor in the design of our imaging system. In this analysis I have not taken into account the attenuation factor characteristic of acousto-optic materials. In practice the effect of the material attenuation will be to lower the MTF of the Bragg cell in the case of large apertures. We also assumed that the Bragg cell was illuminated with a light beam of uniform intensity. Very often, however, laser beams will have a Gaussian profile which alters the Bragg cell MTF for a given aperture. A derivation of Bragg cell MTF's which includes the effect of attenuation and light distribution across the aperture can be found in ref. 45.

Throughout this analysis I have modeled the human eye as a diffraction limited optical system, and I have also assumed the visual system to be equally sensitive to all spatial frequency components of an image. These assumptions are clearly inaccurate, and a more complete model should take into account the spatial frequency response of the human visual system.

V SYSTEM DESIGN

5.1 Objectives

The previous two chapters have laid the foundation for a new generation of large sized displays. The first generation system was capable of displaying $3 \times 2^{21} = 6.29$ million samples. The overall objective of the second generation display has been to increase the total capacity of the display by a factor of six to bring the total number of samples to a number close to 38 million. As I have explained in chapters 3 and 4, the only practical way to attain those figures is to make use of parallelism at both the image and Fourier transform planes.

This chapter will cover the implementation of the second generation of holographic video displays. It should be noted that such an implementation was done progressively over a period of two years. For the sake of simplicity, however, I will describe only the final version of the system as is stands now (April 1994). Describing the display in its previous incarnations would add little scientific or technical content to this thesis.

I will concentrate exclusively on the electro-optical portion of the display in this section. The computation of the holographic fringes used in the display is a fascinating topic by itself, and the reader is referred to ref. 19 for more information on that subject.

5.2 Selection of a suitable display driver

The radio-frequency bandwidth of the signals sent to the Bragg cells determinate the optimum Bragg cell material to be used. That bandwidth is primarily determined by the architecture of the display driver. Since a Bragg cell based display has no memory each complete frame should be refreshed at a rate sufficient to avoid flicker (in practice, above 30 frames/s, although 60 frames/s is a more desirable number). The total sample rate S of the display electronics is thus equal to:

$$S = \frac{N^{samples}}{\tau^{frame}} \tag{5.1}$$

where τ^{frame} denotes the period of a single frame. A 38 million samples image refreshed at 30 frames/s will thus require 1.14 billion samples per second. This is equivalent to a total data rate of 9.12 Gbits/s if we assume 8 bits per sample. An additional constraint is that the samples must be read without interruption during each line scan, which typically consists of hundred of thousands of samples. Any significant gaps in the bit stream would be readily visible on the image plane.

No commercially available display driver can output 1.14 billion samples/s, which is the motivation for using a parallel approach. At the time of the design (Fall 1990), systems built by Metheus and Univision could achieve rates of 360 to 400 Msamples/s, but discussions with the technical staff of those companies rapidly convinced us that this option was not practical. The main problem with these systems came from the fact that they could not be reconfigured to output long uninterrupted data streams.

Fortunately another group at the Media Laboratory was at the same time developing a high bandwidth framebuffer for use in a digital video processing system. One outstanding characteristic of the so-called CHEOPS framebuffer comes from its extreme flexibility in producing different types of video signals[46]. This flexibility is due to the extensive use of programmable array logic chips (PAL's) in the control circuitry and to the fact that a large number of display parameters can be modified by software. Indeed we found that relatively straightforward modifications in the PAL programming and in the display software could render the CHEOPS framebuffer suitable to the display of holographic images. In particular the display could be reconfigured to output uninterrupted data streams of an arbitrary length.

Many problems were still present, however. The first problem was that the initial design could not allow the synchronous operation of multiple cards. The solution to this problem was to distribute the display clock so that all framebuffer cards could be run as slaves from a single master card.

The implentation of this scheme was in practice quite difficult because of the high frequency (110 MHz) of the display clock. Another problem was that the CHEOPS processor card was originally designed to address a maximum of four output modules. This problem was solved by addressing additional output cards as input cards and modifying the controller firmware consequently. For more details on these modifications the reader is referred to ref. 47.

Each CHEOPS framebuffer board has three output channels, which are normally used to drive the red, green, and blue pixels of a video monitor. Each of these channels comprises a digital to analog converter (DAC) having 8 bits of resolution. Each framebufffer channel accesses 2^{21} = 2.1 million bytes of video random access memory. Thus the fulfillment of our initial goal requires 38 / 2.1 = 18 output channels equivalent to 6 framebuffer boards.

5.3 Display parameters

Each one of the display driver channnels accesses 2.1 Mbytes of memory. We now have to determine the image format that will produce the best visual results when using the full display memory.

A first constraint comes from the architecture of the CHEOPS display driver that makes it considerably more efficient in manipulating data blocks being powers of 2. We also were seeking a vertical resolution superior to 100 lines, a horizontal size of around 150 mm, and a horizontal view angle superior to 20 degrees. A few calculations convinced us that the most suitable number of pixels per scan line was equal to 2^{18} = 262144 pixels. Choosing a horizontal size of 150 mm will then result in a horizontal view zone of 33 degrees if we refer to equation (1.3) and assume an illumination wavelength of 633 nm (HeNe laser). The number of display lines is then equal to $18 \times 2^{21} / 2^{18}$ = 144 lines, a figure which is comparable to the NTSC standard for broadcast television.

5.4 Selection of Bragg cell parameters

5.4.1 Bragg cell materials

The 110 MHz sampling rate of the CHEOPS output circuitry implies a maximum analog bandwidth of 55 MHz by virtue of the Nyquist theorem. We are now faced with the task of finding the optimum material on which we can multiplex 18 of those channels.

If we refer to Chapter 2, the most attractive materials for multichannel operation are the ones exhibiting some degree of self-collimation, such as shear mode GaP or longitudinal tellurium dioxide. It is thus logical to consider these materials first.

At design time, good quality gallium phosphide crystals cut along the shear mode propagation axis were not commercially available. Moreover, GaP is only transmissive in the red portion of the spectrum, which excludes its utilisation for color displays.

The next two candidates, longitudinal mode TeO_2 and shear mode TeO_2 , have a long history of use in multi-channel Bragg cells. High quality crystals of adequate sizes are commercially available from a number of vendors.

5.4.2 Longitudinal vs shear mode TeO_2 Bragg cells

A side by side comparison of Bragg cells based on those two materials greatly simplifies the selection task; I will first treat the longitudinal mode TeO_2 case. In the remainder of this chapter the suffixes x and y will denote quantities measured along the horizontal and vertical axes respectively.

The angular range of light diffracted by the AOM is found by combining equations (1.1) and (2.1):

$$\Delta\theta^x = \frac{\lambda \Delta F}{V} \tag{5.2}$$

and the angular range in the image plane is related to (5.2) by the magnification M_t^x of the optical system:

$$\Delta\theta_i^x = \frac{\Delta\theta^x}{M_t^x} = \frac{\lambda\Delta F}{M_t^x V} \tag{5.3}$$

using condition (2.9) to determine the necessary size of the display and combining it with (5.3) results in the expression:

$$D > \frac{\Delta\theta_i^x V}{\lambda\Delta F}\frac{sz_{max}}{(z_{obs} - z_{max})} \tag{5.4}$$

In the case ouf our system with a 55 MHz analog RF range the angular range will be restricted to 0.47 deg. Thus a 30 deg. image plane view zone will require a magnification factor of 1/63. With z_{max} = 100 mm, s = 3 mm and a viewing distance of 600 mm the minimum required Bragg cell length is thus 38 mm.

The minimum scan time τ of a single line will be equal to 2^{18} / 110 10^6 = 2.4 ms. Since the output imaging lens limits the optical scanning range at the Fourier plane to±15 degrees the necessary angular speed of the deflecting element is equal to 30 / (0.0024 x 2) = 6250 deg/s = 109 rad / s. The focal length of the Fourier transform lens is then determined with the help of (2.5) since we have chosen a confocal geometry. The use of longitudinal TeO_2 with an acoustic velocity of 4.26 km/s results in a Fourier transform lens having a focal length f^x_{ft} = 9.8 m.

The minimum necessary height H of the transducer is found by solving equation (3.4) while taking into account the effect of the anisotropy factor b. This results in the expression:

$$H = \sqrt{D\Lambda(1-2b)} \tag{5.5}$$

where we have assumed a rectangular shaped transducer for the sake of simplicity. A 75 MHz center frequency longitudinal mode TeO_2 crystal having an aperture of 38 mm thus requires a transducer height of 1 mm. The criterion that the interchannel isolation be greater than 20 db over the length D implies an aperture to spacing ratio of 1/3, which signifies that the acoustic channels will be spaced 3 mm apart. The crystal will thus have a height H^{tot} of 3 x 18 = 54 mm. The same calculation with shear mode TeO_2 yields the following results, which are displayed in Table 5.1:

material	$\Delta\theta^x$ (deg.)	D (mm)	H (mm)	H^{tot} (mm)	M_2	f_{ft}^x (m)
TeO_2 (long.)	0.47	38	1	54	34.5	19.5
TeO_2 (shear)	3.23	6	1.56	84	793	2.83

Table 5.1 Multichannel Bragg cells parameters

Discussions with Bragg cell manufacturers confirmed that both types of Bragg cells were indeed feasible in the specified dimensions although this involved stretching the state of the are in crystal growing techniques. I decided on the use of the shear mode material in the final design for the following reasons:

- The figure of merit M_2 of the shear mode material is 23 times higher than for the longitudinal mode, which according to equation (3.1) implies that the required driver power is 4.7 times smaller.
- The focal length of the Fourier transform element is considerably shorter, which significantly simplifies the design of the optical system.
- Previous generations of the display were implemented with shear mode TeO_2, which resulted in considerable practical experience with this material.

The longitudinal mode material, however, becomes more attractive at higher bandwidths and probably represents the better alternative for large sized displays.

NEOS Corp. (Melbourne, FL) was selected as the Bragg cell provider. The initial design was for a Bragg cell having dimensions H^{tot} = 75 mm and D = 12 mm (a larger space bandwidth product

than the minimum necessary was chosen as to allow with future experimentation with very deep images or other display geometries). However, problems encountered during crystal growth required limiting the height of the crystals to 67 mm. The height of each transducer was chosen equal to 1.5 mm and the distance between transducer centers equal to 4 mm. Through the use use of carefully apodized diamond shape electrodes the manufacturer was able to maintain an inter-channel isolation greater than 25 db across the length of the Bragg cell.

5.5 Fourier plane scanning

5.5.1 Scanning element requirements

The 2.4 ms active scan time per line would imply driving the scanning elements with a sawtooth having a frequency of 420 Hz if no retrace time were present. In practice, however, the mechanical inertia of the scanning elements implies the addition of a retrace interval after each horizontal scan line. This inactive retrace interval results in a lower display refresh rate, and should thus be kept at a minimum.

The speed and precision of the Fourier plane scanning places severe constraints on the scanning elements. Those constraints can be stated as follows:

- Mechanical deflection range in excess of 15 degrees.
- High speed and low inertia.
- High linearity and repeatability.
- Low thermal drift and long term drift.
- Small body size, allowing for a dense packing of the array elements.

5.5.2 Scan configuration

Evaluation of different galvanometric scanners on the market led to the selection of the model 6350 from Cambridge Technology, Watertown, MA. However, calculations based on the galva-

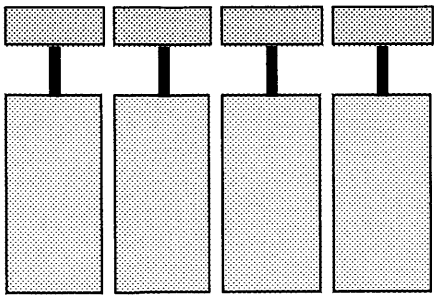

Figure 5.1 Row of galvanometric scanners

nometer size and inertia demonstrated that a simple juxtaposition of the scanning elements Figure 5.1 would not result in an acceptable performance. The array scheme of Figure 5.1 requires individual mirrors of a width at least equal to the galvanometer body's width. The inertia of fused silica mirrors having this dimension would be significantly higher than the galvanometer rotor's, resulting in a considerable degradation in the scanning system's frequency response.

The use of beryllium mirrors was considered to solve this problem. However, beryllium mirrors are extremely expensive, with a cost per unit higher than a galvanometer. It was thus decided to use the scanning elements in the configuration of Figure 5.2. Although more complex, this configuration allows to halve the mirror width and presents the advantage of reducing the intermirror gap as per equation (4.8).

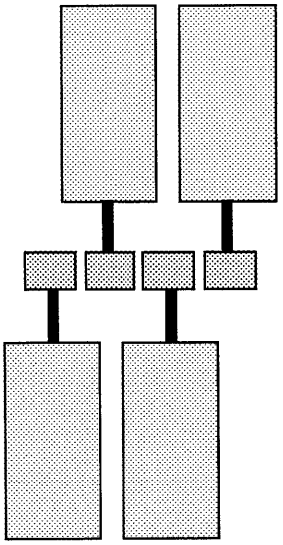

Figure 5.2 Alternate arrangement of galvanometric scanners.

The configuration of Figure 5.2 results in mirrors having a width of 20 mm. Their height was selected to avalue of 6 mm after evaluation of the vertical scanning requirements (which will be discussed later in this chapter). Each fused silica mirror is 3 mm thick, which results in a mirror distortion of less than 1/4 wave during scanning.

The galvanometers are mounted on a thick aluminum plate which also serves as a heat sink. The array operation requires that the mirrors stay in excellent angular registration thorough the scanning range, a task that stretched the patience of the author. The most challenging task was to dynamically register the mirrors, a process that involved a careful adjustment of the servo response of each galvanometer.

The response of the scanning elements was carefully analyzed to determine the optimum scanning waveforms and frequencies. It became quite evident that a traditional raster type of scanning (which uses sawtooth waveforms to drive the galvanometers) could not be implemented at reasonable frequencies because the slew rate of the actuator would imply long retrace intervals and consequently unacceptedly low refresh rates. It was then decided to drive the scanning elements with triangular waveforms, and to use both scan directions as active write intervals. This so-called *boustrophedonic* configuration minimizes the inactive scan time and thus results in acceptable refresh rates. Its main inconvenient comes from the need for two sets of Bragg cells, each driven from opposite sides during alternate lines.

The size of the Fourier transform is given by the equation:

$$\Delta x = \frac{\lambda f^{x}_{ft} \Delta \nu}{v} \tag{5.6}$$

and is thus equal to 145 mm with a TeO_2 Bragg cell having a 50MHz bandwidth in the configuration described in section 5.4.2. This configuration thus requires 7 scanning elements of the above type.

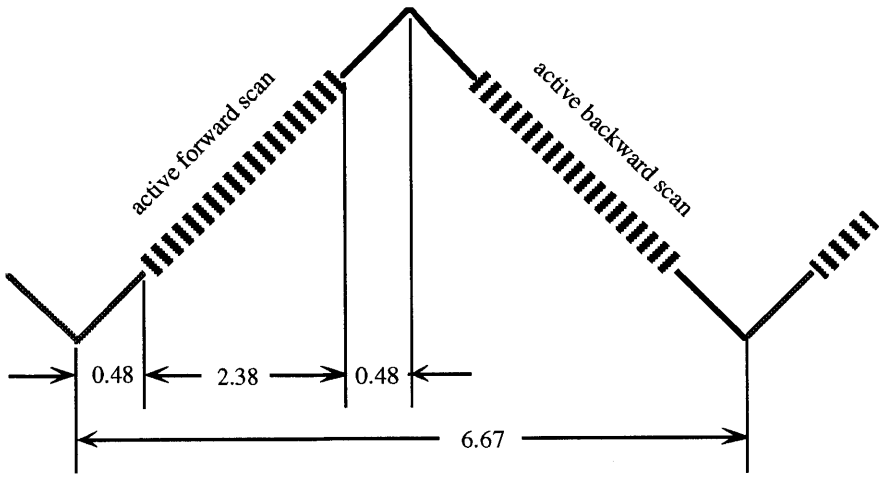

Figure 5.3 Horizontal scanning waveform. Time intervals are in milliseconds.

5.5.3 Horizontal scan format

Even the triangular scan format requires a significant inactive interval since we are interested in using only the linear portion of the scan. After a series of experiments I decided on the format described in Figure 5.3.

The active scan time per horizontal line is determined by the CHEOPS firmware to be equivalent to 2.4 ms. There are two active intervals per scan period. The scan frequency is set to 150 Hz, which signifies that there will be a 0.9 ms inactive period between each active interval. The active duty cycle per horizontal line is thus equal to 73%.

As derived in Section 5.4.2, a 30 degrees optical range is deflected during an active interval during which each mirror rotates at a constant velocity of 109 rad/s. The total mechanical excursion, including inactive intervals, is equal to 18 degrees.

A total frame includes $2^{21} / (2 \times 2^{18}) = 4$ complete active scan periods. An inactive period is added after each frame as a vertical retrace interval. The display refresh rate is thus equal to 150 / (4 + 1) = 30 Hz, which is acceptable in terms of flicker.

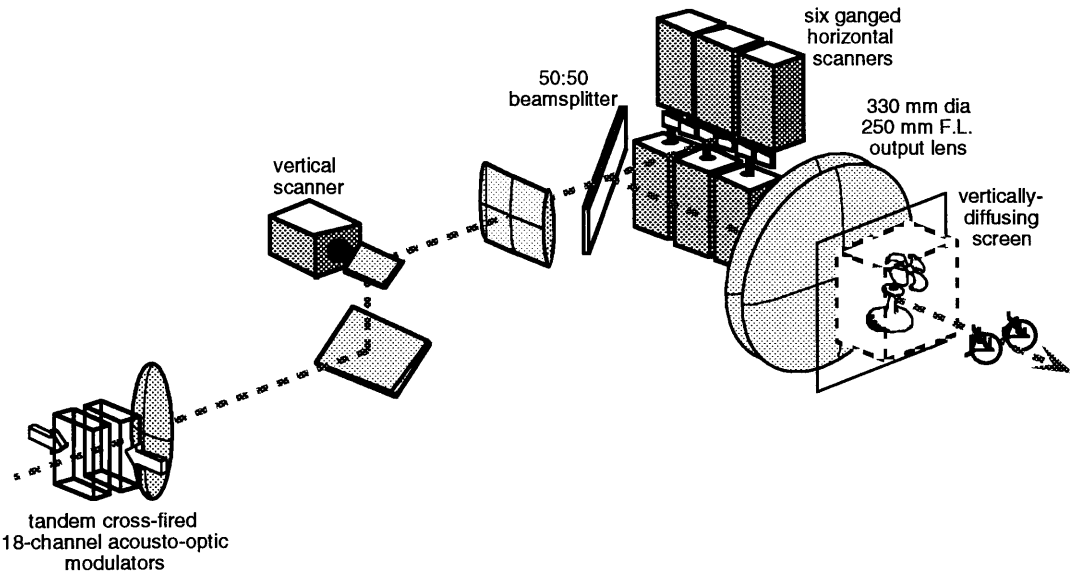

Figure 5.4 Simplified drawing of the holographic video display

5.6 Optical geometry (Horizontal axis)

5.6.1 Beam shaping optics

A schematic drawing of the horizontal display optics is presented in Figure 5.5. A simplified perspective drawing of the overall display geometry is presented in Figure 5.4. The horizontal axis beam shaping optics consist of a simple beam expander composed of lens L_2 and L_3. The telescope formed by those lenses magnifies the 2 mm diameter input laser beam by a factor of 7.5. The central portion of the collimated expanded beam illuminates the two Bragg cells.

5.6.2 Bragg cells

The geometry of each Bragg cell has been described in section 5.4.2. The Bragg cells are placed back to back with their surfaces almost touching each other (this feature was included in the original design). Their orientation with respect to the laser is chosen to satisfy the Bragg condition at the center frequency and is then fine tuned to get the flattest possible response across the passband (50 - 100 MHz).

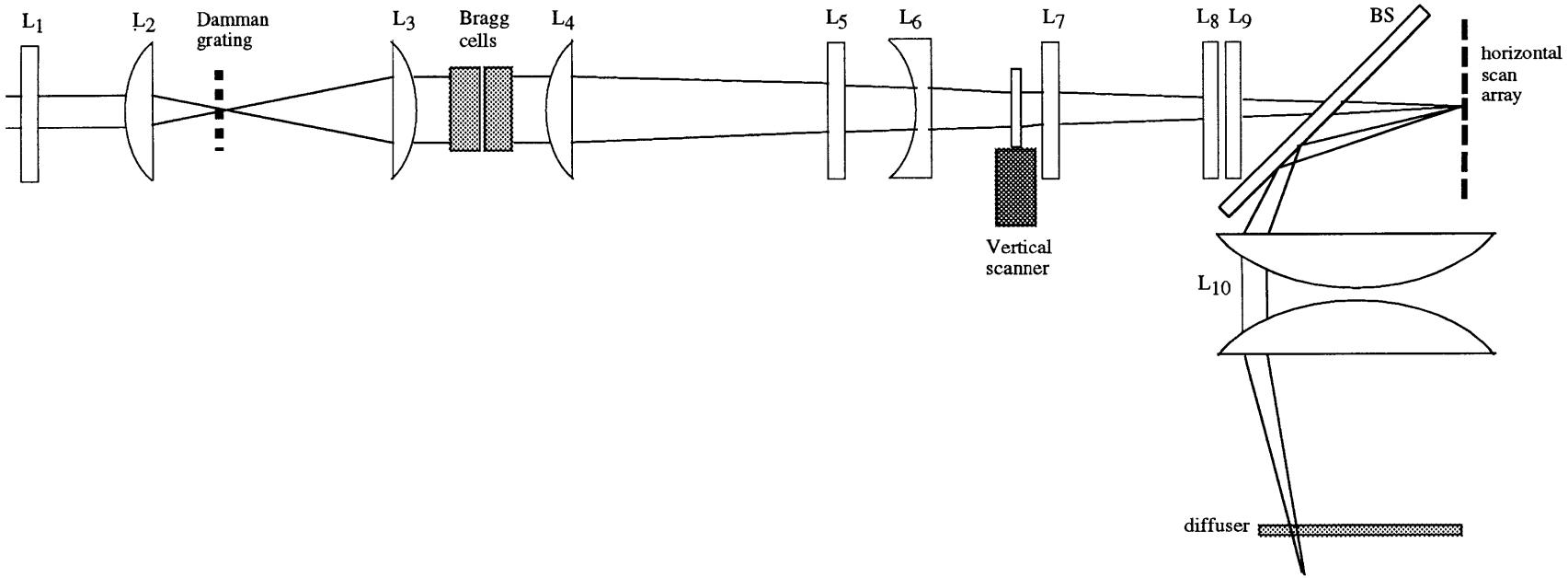

Figure 5.5 Top view of the display optics. Lenses L_3, L_4, and L_{10} are spherical. Lenses L_2 and L_6 are cylindrical and have power in the horizontal axis. L_1, L_5, L_7, L_8, and L_9 are cylindrical and have power in the vertical axis.

5.6.3 Fourier transform optics

The calculations of section 5.4.2 imply that the Fourier transform lens must have a focal length f_{ft} = 2830 mm. This number is of course quite impractical if implemented with a single lens. It was thus decided to use two lenses L_4 and L_6 in a telephoto combination. Elementary geometrical optics prescribe the distance z_{46} between L_4 and L_6 :

$$z_{46} = f_4 + f_6 - \frac{f_4 f_6}{f_{ft}} \qquad (5.7)$$

and the total distance $z_{4ft'}$ between L_4 and the Fourier plane is given by:

$$z_{4ft} = \frac{f_6 (f_4 - z_{46})}{f_4 + f_6 - z_{46}} + z_{46} \qquad (5.8)$$

With f_4 = 600 mm and f_6 = -150 mm we thus get z_{46} = 482 mm and z_{4ft}= 1035 mm. Using a telephoto combination thus results in a considerable improvement in the display footprint.

5.6.4 Output imaging lens

The focal length of the imaging lens L_{10} is determined by equation (2.6). I chose a value of 275 mm which results in a horizontal view zone of 30.2 degrees for a 50 MHz analog bandwidth signal sent to the Bragg cell.

The diameter D of the imaging lens is given by the equation[2]:

$$D = 2 f_{10} \tan\left(\frac{\theta_{scan}}{2}\right) + \frac{\lambda f_{ft} \Delta\nu}{V} \qquad (5.9)$$

For the values mentioned above, an imaging lens having a diameter of 295 mm is thus required. The very low f/number of the lens implies that it should be a multi-element lens. The design and fabrication of the lens was contracted to an external source (Optikos Corp, Cambridge, MA). The

final design consists essentially in a doublet of two plano-convex lenses with the planar surfaces facing the conjugate focii. Its active aperture when mounted is 320 mm. The doublet is mounted in a black anodized aluminum barrel.

5.7 Optical geometry (vertical axis)

5.7.1 Beam shaping optics

Because the fill ratio of the acoustic channels is about one third, it would be quite inefficient to illuminate the crystal aperture by just vertically expanding the incoming laser beam. It was thus decided to individually illuminate each acoustic column with a properly shaped beam. The optical system described in Figure 5.6 performs the desired beam shaping operation. The key element in this configuration is a Damman grating manufactured by the National Institute of Optics (Quebec, Canada), which separates the incoming beam into 19 orders of equal power. The angular separation between each order is equal to 50 milliradians. The Damman grating is placed in the confocal plane of lenses L_1 and L_3. Choosing the focal length of L_3 equal to 300 mm results is a vertical stack of light sheets spaced 4 mm apart, which corresponds to the interchannel spacing of the Bragg cell. The thickness of each sheet is determined by the width of the incoming beam times

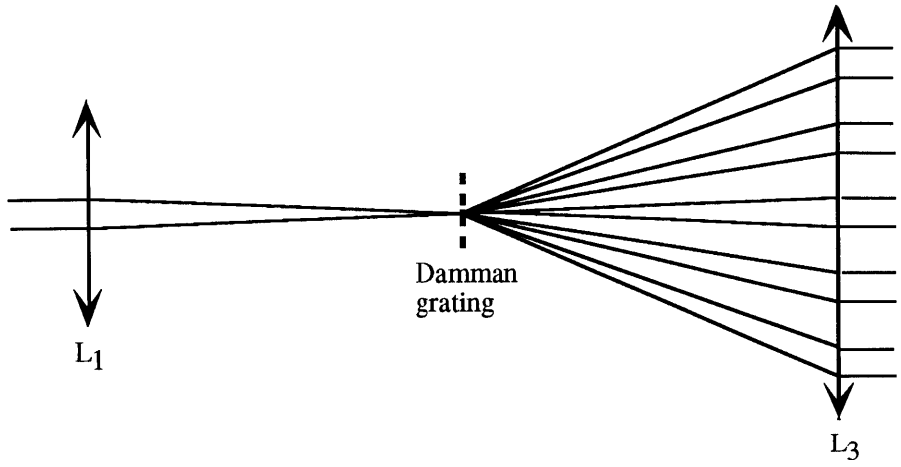

Figure 5.6 Splitting an incoming beam into multiple collimated beams with a Damman grating

the magnification of the L_1-L_3 telescope. Since the acoustic width is about equal to the laser beam diameter a unit magnification is chosen, and thus $f_1 = f_3 = 300$ mm. The Bragg cells are adjusted so that the light sheets and the acoustic columns are correctly registered

5.7.2 vertical scanning

The vertical scanning subsystem is similar to the description given in section 2.2.5. A detailed shematic is provided in Figure 5.5. Lenses L_4 and L_5 focus the light diffracted by the Bragg cell on the surface of the vertical scanning mirror. A cylindrical doublet L_7 placed immediately after the mirror determines the vertical focal plane of the scanned array in the image plane. The cylindrical doublet L_8 - L_9 images the vertical scanning mirror on the horizontal scanning plane. The output lens L_{10} then images the Bragg cell array in the center of the image plane. The vertical transverse magnification is essentially determined by lenses L_4, L_5, and L_{10} and is approximately given by the formula:

$$M_t^y \approx f_{10}\left(\frac{1}{f_4} + \frac{1}{f_5} - \frac{z_{45}}{f_4 f_5}\right) \tag{5.10}$$

It was decided at the design stage to set the aspect ratio of the image equal to 2:1, (equivalent to the aspect ratio of the ShowScan cinematographic process and close to adopted standard for HDTV), thus implying a vertical image size of 75 mm. The image of the Bragg cell is sweeped 8 times per frame (4 times forward an 4 times backward) and thus the required magnification ratio is equal to 75 / (8 x 67) = 0.14.

The vertical scan is of a conventional sawtooth type, non interlaced, at a 30 Hz rate. The retrace interval is equivalent to a full horizontal scan interval (6.66 ms). A galvanometer motor identical to the ones used in the horizontal scanning (Cambridge Technology model 6350) was selected, with a scanning mirror having dimensions of 60 (along the scan axis) x 7 x 3 mm.

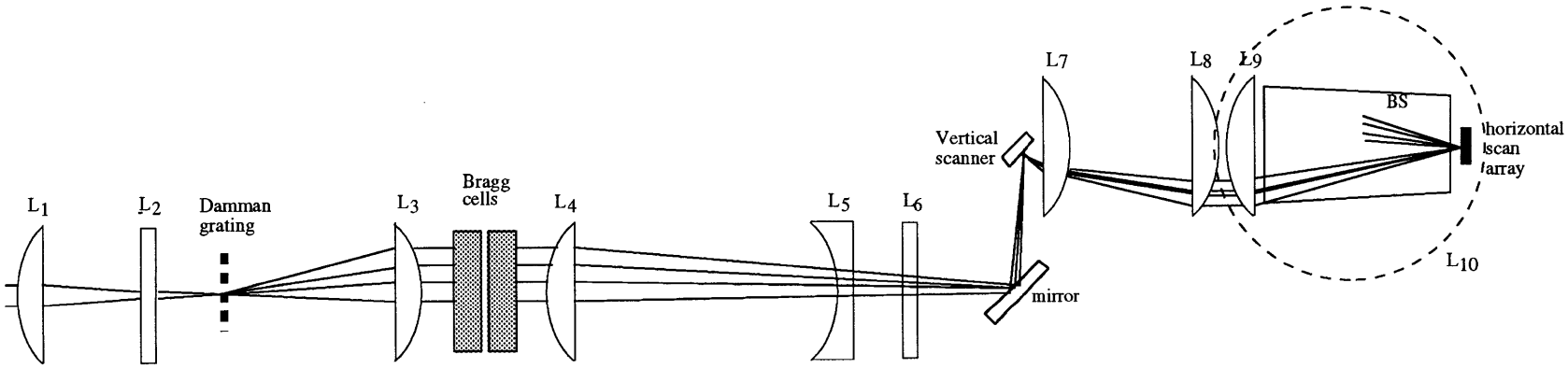

Figure 5.7 Side view of the display optics. Lenses L1, L3, L4, L5, L7, L8, L9, and L10 are cylindrical and have power in the vertical axis. The vertical diffuser has been omitted for clarity.

5.7.3 Vertical diffuser

The horizontal parallax only nature of the display requires a diffusing element in the image plane. The function of this diffuser is to scatter light along the vertical axis while leaving the horizontal content of the image unaltered. The final version of the display uses a one dimensional holographic diffuser manufactured by Physical Optics Corp, Torrance, CA. The total angle of diffusion is 30 degrees in the diffusing direction. This diffuser exhibits extremely low scatter along the non diffusing axis and proved very satisfactory for our purpose.

5.8 Display electronics

5.8.1 RF signal processing.

Figure 5.8 shows a block diagram of the RF processing circuitry. The signal coming from the CHEOPS framebuffer is first filtered to keep the lower sideband and then mixed with a 100 MHz local oscillator which upconverts it to a signal having a frequency range adequate for the Bragg cell (50 - 100 MHz). The upconverted signal then goes through a variable attenuator whose purpose is to equalize the optical power coming out of each Bragg cell channel. The signal is then amplified and filtered to keep the lower of the two sidebands resulting from the upconversion.

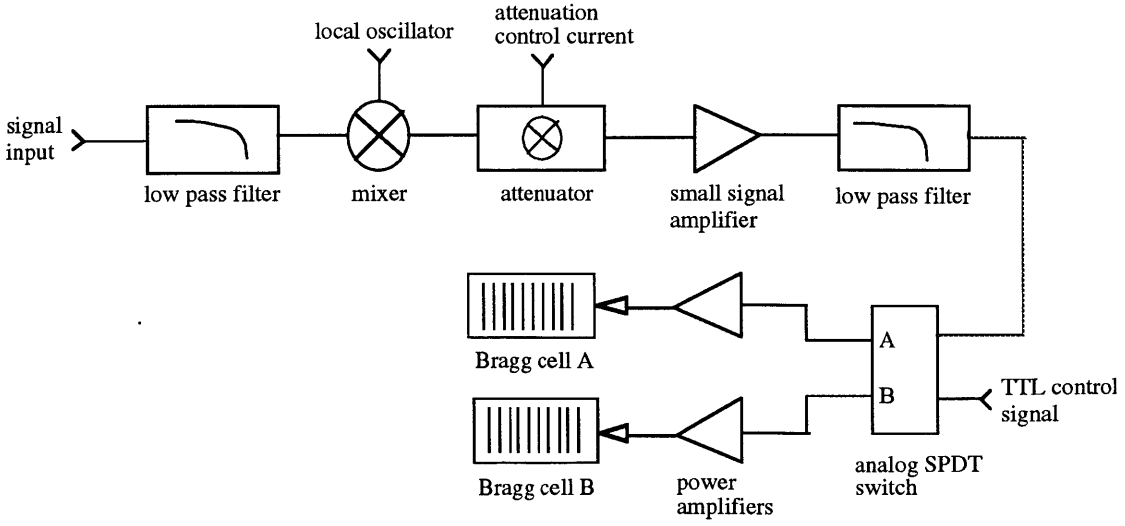

Figure 5.8 Block diagram of the RF processor

Since each Bragg cell is active only during one half of a scan period an electronic SPDT switch routes the RF signal to the corresponding active cell. The demultiplexed RF signals then go through a set of power amplifiers before being sent to the Bragg cells.

The signal processing system is implemented on standard two sided printed circuit boards. The circuitry corresponding to two complete channels is built onto each board. Each board is enclosed in an aluminum case which limits the amount of radio frequency being radiated and serves as a heat sink for the power amplifiers. The cases fit into a standard rackmount cage where 3 box fans help dissipate the large amount of heat (400 watts) dissipated by the power amplifiers.

5.8.2 Generation of scan signals

5.8.2.1 *Horizontal scan signals*

The generation of the control signals is considerably simplified from the fact that the CHEOPS framebuffer generates its own separate h-sync and v-sync signals. The h-sync signal is sent directly to the phase lock input of a high quality digital function generator (Hewlett Packard #3314A) which is set to generate a triangular wave of the correct amplitude. The phase relation between the sync input and the triangular scan signal is directly set on the signal generator. The triangular waveform is then sent to the horizontal scan servo amplifiers.

A divide-by-two counter also processes the CHEOPS h-sync pulse into a 50% duty cycle square wave of a period equal to a scan interval (6.67 ms). This square wave is used to control the demultiplexing switches of the RF signal processor. An inverter and switch combination determines which Bragg cell is active during each scan direction. A detailed drawing of the control circuit is shown in Appendix C.

5.8.2.2 *Vertical scan signals*

The vertical scan signal is generated by incrementing a counter at every h-scan pulse. The outputs of the counter are connected to a digital to analog converter (DAC) and the counter is cleared by

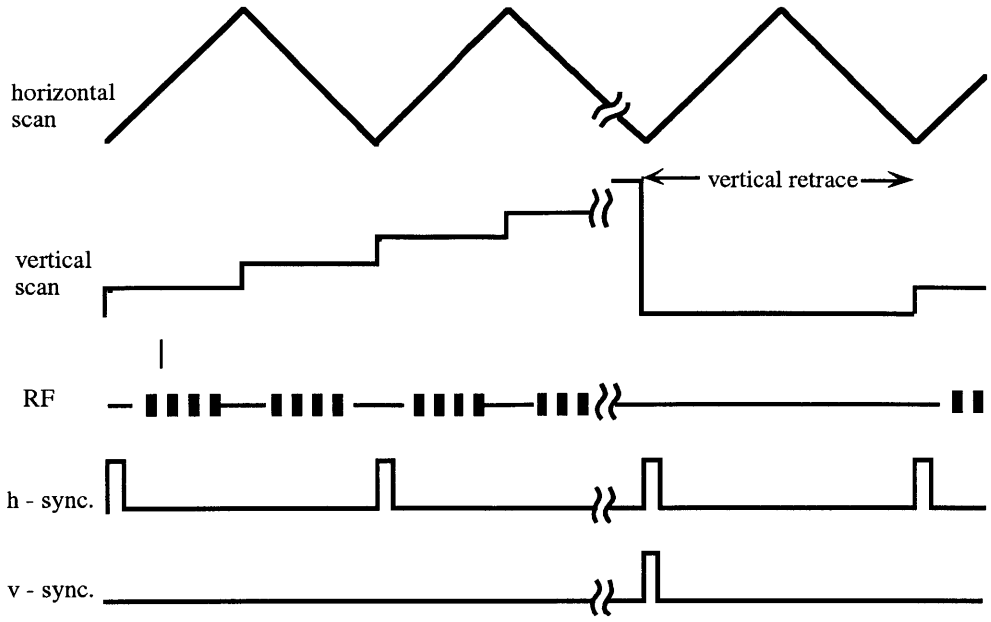

Figure 5.9 Signals used to drive the holographic display.

the CHEOPS v-sync pulse. The signal coming from the DAC is thus a discrete sawtooth in which each step correspond to a horizontal scan interval. This signal is then sent to the vertical scan servo amplifier with a correct amplitude and offset.

VI RESULTS

6.1 Image size and view zone

The final version of the display was implemented with 6 scanning elements in the Fourier plane. The useable portion of the RF spectrum thus extends across a 42 MHz bandwidth. The measured size of the image is equal to 150 x 75 mm. The depth of field is essentially limited by the amount of astigmatism that the human eye can tolerate (about 300 mm at a normal view distance). The vertical resolution is equal to 144 lines. A picture of a typical holographic image is shown in Figure 6.1.

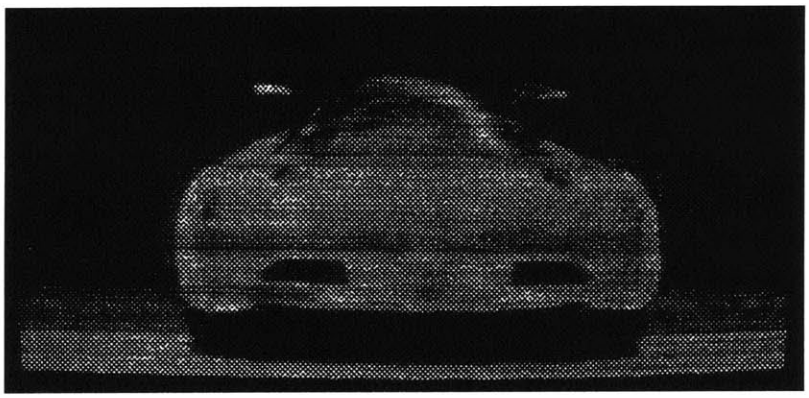

Figure 6.1 Holographic still image of a Honda EPX. Wendy Plesniak rendered the image and Mark Lucente computed the hologram fringes.

6.2 Resolution

6.2.1 Vertical resolution

The vertical resolution is determined by the number of scan lines per unit length. In the final version of the display this equates to 75 / 144 = 2 lines/mm, a figure roughly equivalent to the vertical resolution of an average NTSC monitor. The vertical lines do not blur into each other. Indeed, a close inspection of the image reveals that successive scan lines are separated by a narrow gap (Figure 6.2). At a normal viewing distance this gap is barely noticeable.

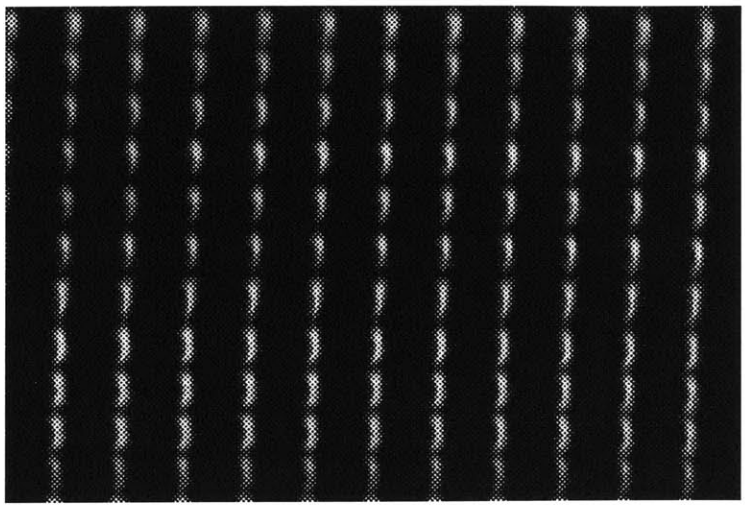

Figure 6.2 Close-up of the central part of the preceding image. The size of the enlarged area is 6.4 x 4.8 mm

6.2.2 Point spread function (horizontal axis)

The horizontal axis PSF was determined by placing a CCD array directly in the image plane after having removed the vertical diffuser. This CCD array has almost square pixels of a size equal to 8.33 x 9.71 micrometers. Only one galvanometric scanner at a time was illuminated to eliminate the effects of mirror misregistrations. The video frames coming from the array were digitized by a Sirius video frame grabber installed in an SGI ONYX workstation. A vertical array of points was calculated at different z-planes, both on and off axis, to evaluate the behavior of the PSF. Figure 6.3, Figure 6.4, and Figure 6.5 give a detailed view of the PSF at those planes.

The PSF along the horizontal axis is quite similar for on-axis and off-axis points, and stays fairly constant with respect to depth. In the vertical direction the scan lines come to a focus only at the Bragg cell plane (where the diffuser would normally be). From Figure 6.4 we can deduce the half intensity width of the PSF to be equal to 70 micrometers. A calculation using equation (4.24) gives a figure of 15 micrometers. It is thus clear that the optical system is far from being diffraction limited.

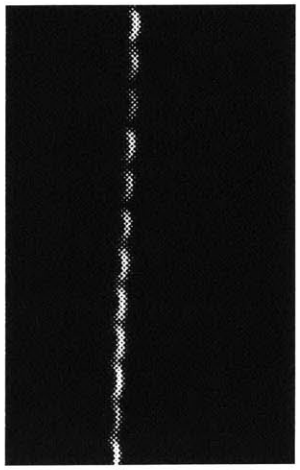

Figure 6.3 Enlarged section of a single vertical line. The line is imaged on-axis and is 3 mm from the plane of the Bragg cell in the image space. The size of the area is 2.5 x 4.6 mm.

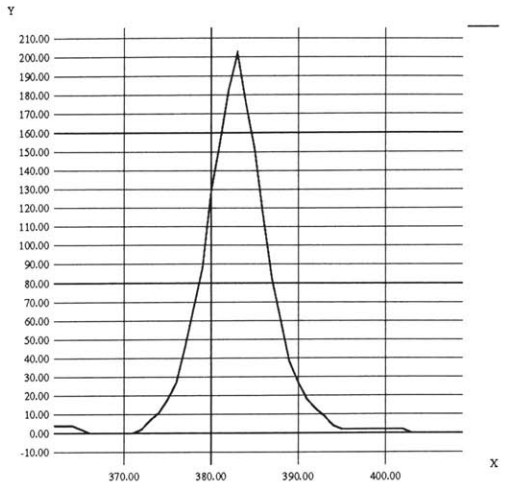

Figure 6.4 Plot of the central section of Figure 6.3. The X axis represents the pixel count and the Y axis the relative intensity. Each pixel is 8.3 microns wide.

The aberrations which spread the PSF imply that the optics do not be behave exactly as predicted in Chapter IV. Indeed, in a system with aberrations the PSF usually narrows as the aperture is reduced (up to a point where pupil diffraction effects take over), which is opposite to the case of a diffraction-limited system. At any usual viewing distance the pupil of the observer is considerably smaller than the projection of the system pupil in the Mark II display. The consequence of this is that the angle subtended by a single point will always be smaller than 70 / D_{view} μradians where D_{view} is the viewer's distance. The minimum comfortable viewing distance for a human observer is about 20 centimeters. Thus the angle subtended by a point will always be smaller than 1 minute of arc, which is the resolution limit of the human eye.

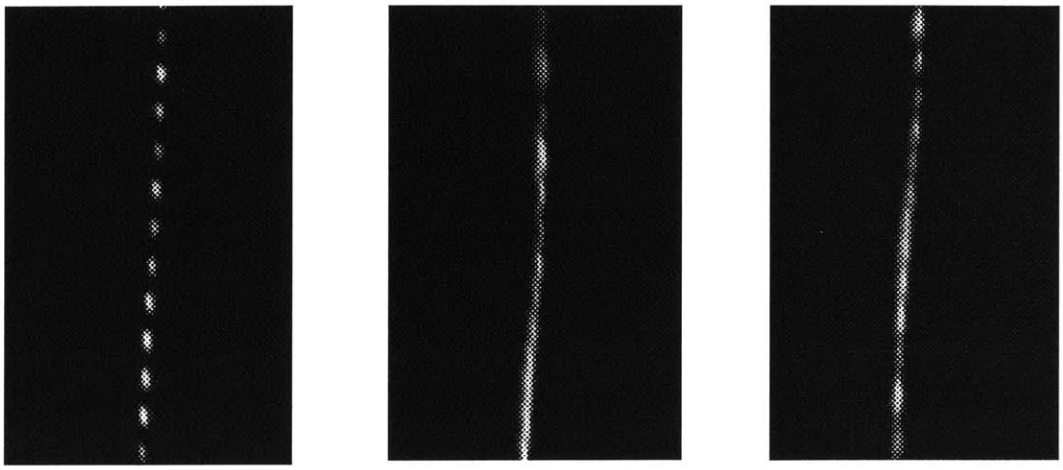

Figure 6.5 left image: off axis close-up of a single vertical line situated 3 mm from the image of the Bragg cell. Center image: on-axis vertical line, 5 cm away from the Bragg cell plane. Right image: off axis vertical line, 5 cm away from the Bragg cell plane. All off-axis images were calculated to be 6 cm away from the optical axis. The size of the area is 2.5 x 4.6 mm in all three cases.

6.3 Contrast ratio

The contrast ratio in this type of display depends strongly on the type of image being represented. This stems from the fact that the dynamic range of the Bragg cell is shared by adjacent image sections when the scene to be represented moves away from the Bragg cell plane. Single points (corresponding to specular reflections) imaged away from the image plane can be extremely bright, but also lead to intermodulation noise problems (detailed in the following section), and are thus usually either avoided or attenuated (this is also the case in optical holography). The vertical lines of Figure 6.5 are examples of such specular images.

A realistic situation can be simulated by measuring the contrast between a uniform diffuse patch a few millimeters across and the surrounding field. Such a diffuse patch was calculated using a pseudo-random diffuser algorithm. The measurements were carried out using a Newport light meter placed at the plane of the Bragg cell image. For a single uniform patch the measured ratio was equal to 70. Similar measurements carried out on the EPX image of Figure 6.1 yielded similar results.

6.4 Noise

6.4.1 Intrinsic vs system noise

Two principal types of noise can be defined when analysing the image: Intrinsic noise and system noise.

The intrinsic noise derives from the physics of the display and can thus never be eliminated, although its inluence can be minimized by being careful when computing the holograms. This type of noise is well characterized and can be calculated. Quantization noise and intermodulation noise fit into that category.

System noise derives from various factors such as reflections on lens surfaces, scattering by dust particles on optical surfaces, and noise coming from the processing electronics. Very often these sources of noise will affect some parts of the image more than others (this is especially true from lens reflection artefacts).

6.4.2 Intrinsic noise

6.4.2.1 Quantization noise

Quantization noise arises from the finite size of the samples used to represent our images (8 bits/sample in the case of CHEOPS). This is a well known effect in any digital signal processing system. The mean square value of this quantization noise can be shown to be equal to:

$$\langle e^2 \rangle = \frac{d^2}{12} \tag{6.1}$$

where d is the size of a quantization step. Since the maximum signal is $2^n d$ in the case of n bits per sample, the ratio of peak signal to rms noise is:

$$S/N = \frac{2^n}{12} \tag{6.2}$$

For 8 bits per sample this ratio is 887 or 59 db.

The quantization noise spectrum is uniformly distributed across the frequency range of interest . This noise will thus appear as scatter in the final image. It is of a fundamental nature and the only way to reduce it would be to replace the current framebuffer by a model offering more bits per sample. Equation (6.2) thus represents the highest possible theoretical S/N ratio of the display. In practice, however, quantization noise proves to be by far the smallest contributor to the overall noise in our images and can be neglected.

6.4.2.2 Intermodulation distortion.

The Bragg cell is not a linear device. More specifically, the diffracted first order intensity is given by expression (3.1).

For very a small diffraction efficiency value the response of the Bragg cell is almost linear. However the AOM response will be less and less linear as the RF input power is increased.

Intermodulation distortion arises from this nonlinearity in the Bragg cell response. It appears when two signals are added and then pass through a nonlinear system. If the respective spatial frequencies of the signals are f_1 and f_2 then at the output of our system the following terms will be added to the original spectrum:

$$2f_1 - f_2,\ 2f_2 - f_1,\ 3f_1 - f_2,\ 3f_2 - f_1,\ 3f_1 - 2f_2, \ldots \tag{6.3}$$

The first two terms of (6.3) are called third order intermodulation products and are by far the most significant contributors the the overall intermodulation distortion. Their effect on the image shows up as a kind of fuzzy halo or ghost surrounding any bright part of the displayed object. For two

equal amplitude spatial frequencies f_1 and f_2 the power I_{int} in the intermodulation products is described by the relation:

$$\frac{I_{int}}{I_1} = \frac{\eta^2}{36} \tag{6.4}$$

where I_1 is the intensity of the first order diffracted beam and η is the power diffraction efficiency for f_1 or f_2 by themselves. Thus if $\eta = 0.1$ the third order intermodulation products will be down by 35 db relative to the main signal. It is clear from (6.4) that we have to drive our display at low diffraction efficiencies (less than 10 %) if we want a clean image. Unfortunately, light scattering from the various optical surfaces become significant at such low efficiencies, so the final operating point of the Bragg cell is a compromise between intermodulation noise and scatter. This problem is also encountered in optical holography, where intermodulation products are usually labelled "self referencing noise". It can be minimized by avoiding bright, specular reflections in the hologram.

6.4.3 System noise

6.4.3.1 Framebuffer noise

The noise coming from hardware errors in the CHEOPS framebuffer proved to be quite a nuisance in the early parts of the project. It was fortunately gradually brought under control, to the extent that the measured framebuffer noise does not exceed the quantization noise.

6.4.3.2 RF processor noise

The RF processing of the signal inevitably introduces some degradation. Three effects are mainly responsible for this degradation:

- White noise.
- Harmonic distortion.

- Intermodulation distortion.

The white noise mainly comes from thermal excitations in the solid-state electronics. Since we use high quality components and our signals are of a relatively high level (typically from 0 to 25 dbm), this white noise has been measured to be smaller than the quantization noise and thus can be neglected. Its effect, if visible, would be that of a uniform scatter across the image.

Harmonic distortion arises from nonlinearities in the mixers and amplifiers. An harmonic distortion component will have an integral number of times the frequency of the input signal. On the display this would be seen as a ghost image displayed at twice the spatial frequency of the original image. Harmonic distortion is virtually negligible in our system since the frequency range of the Bragg cell is restricted to an octave. Any harmonic term will fall outside the Fourier scanning plane an will not appear in the image.

Intermodulation distortion arises from the same nonlinearities in the electronics. Its visual imact has been described in Section 6.4.2.2. The main contribution to intermodulation distortion in our RF subsystem comes from the mixers. Third order intermodulation products have been measured to be more than 35 db below signal when the input levels are carefully adjusted.

6.4.3.3 Multiple reflections

All the lenses in the optical system were coated with multilayer dielectric coatings, resulting in reflection coefficients inferior than 0.5 % at each air/glass interface. However, the large number of lens surfaces in the system resulted in some sligtly visible reflections usually visible from a narrow angle. Those multiple reflections seem to be the main contributor to the overall display noise.

6.5 Scanning artifacts

6.5.1 Mirror misregistration and intermirror gap

The segmented nature of the Fourier transform scanning scheme introduces scanning artifacts if the scanning elements are not carefully registered both statically and dynamically. In addition the intermirror gap results in a intensity dropoff within a small portion of the spatial frequency spectrum.

The registration errors proved to be impossible to completely eliminate, although careful adjustments resulted in misregistrations which were detectable only by a close examination of the image. It was found that the galvanometers drift slowly with time, resulting in the need to adjust the offset voltages every three months or so. It should be noted, however, that the thermal drifts have become considerably smaller over time.

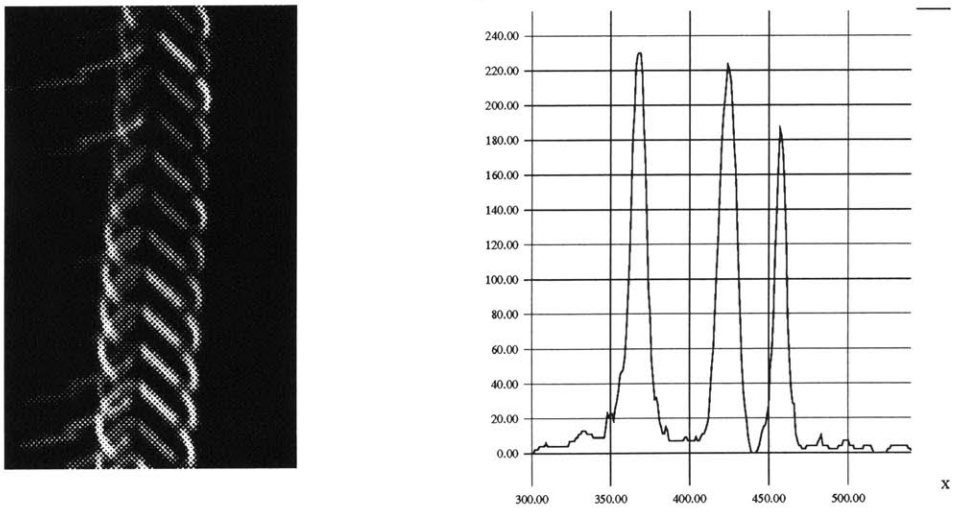

Figure 6.5 Left: Effect of scanning mirror misregistration. The CCD array was put in the image plane while receiving light from the multiple mirrors. The size of the imaged area is 2.5 x 4.6 mm. Right: Plot of the intensity profile across the picture at left. The X axis represents the pixel count and the Y axis the relative intensity. Each pixel is 8.3 microns wide.

This probably the consequence of some form of thermal aging in the scanner armature and associated electronics. A picture of a typical misregistration error is shown in Figure 6.5. In this case the maximum misregistration was equal to 800 micrometers. Misregistration between successive scanning elements is usually considerably lower.

The intensity dropoff due to the gaps proved to be barely perceptible except upon very close examination. This dropoff did not significantly degrade the holographic image.

6.5.2 boustrophedonic scan errors

The boustrophedonic nature of the Fourier plane scanning introduces severe constraints in the linearity of the scanning devices (indeed these constraints are the main reason that type of scan is not used in television). Any velocity differences between the forward and backward scans will show up as discontinuities in the image. Such discontinuities are most visible if the image consists of simple vertical lines, such as in the test pattern of Figure 6.6. It is clear from Figure 6.6 that some degree of nonlinearity is present at the extreme edges of the scan, with typical discontinuities of a few hundred microns. It should be noted, however, that this residual nonlinearity is very difficult to notice in more complex images.

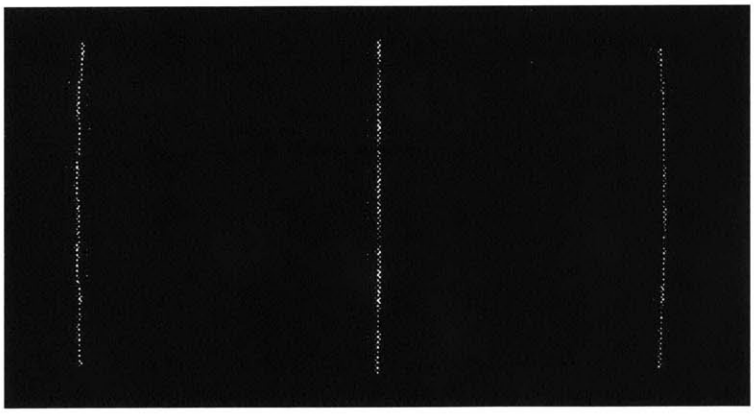

Figure 6.6 Test pattern consisting of one central vertical line and two lines at the edge of the field. The lines are image 3 mm from the Bragg cell plane.

6.5.3 Vertical scanning errors

The vertical scanning element has to perform an angular step after each half scan. The settling time of the scanner creates some small errors visible as gaps between line groups at the beginning of each scan. These gaps are most visible if we image a uniform field and can be discerned at the extreme edges of Figure 6.7. Once again, these artifacts are considerably harder to notice in usual images.

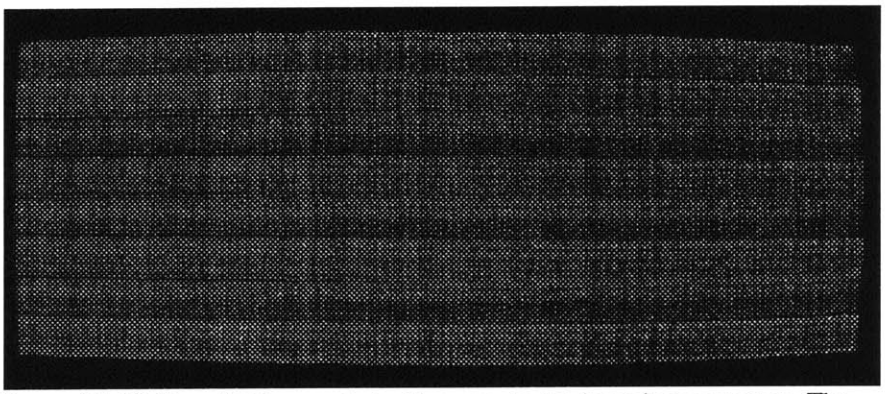

Figure 6.7 Uniform field generated with a pseudo-random phase sequence. The vertical striations are an artifact of the pseudorandom algorithm.

6.6 Distortions

6.6.1 Field curvature

The output plane is slighly curved due to the optical geometry selected and the fact that the output lens consists of only two elements. Without correction the total field curvature is equal to 1 cm. This problem is easy to correct in the horizontal direction by introducing an opposite curvature in the simulated reference beam when computing the hologram. By introducing such a quadratic phase term in the reference beam the horizontal curvature can be rendered negligible. The vertical field curvature is considerably smaller (a few mm) because the output lens works at a larger f/ number in the vertical direction.

6.6.2 Bow scan distortion.

An X-Y scanning scheme consisting of two orthogonal elements will always introduce a form of trigonometric distortion known as *bow scan*[22]. This distortion can be readily noticed in Figure 6.7 as a curvature of the top and bottom of the image. Bow scan can be corrected by various optical schemes usually incorporating the use of a prism. Such a scheme could eventually be implemented in the MIT display but would likely prove quite expensive, requiring the fabrication of a prism having a size comparable to the extent of the Fourier transform.

VII CONCLUSION

The application of parallel architecture principles at every stage in the design has allowed a six-fold increase in display capabilities with respect to previous implementations. An order of magnitude increase in the display space-bandwidth product is still necessary before this technology can be put to practical uses, however. A number of technical problems also need to be solved if this technology is ever to have commercial applications. Some of these problems, as well as a few directions that might help to solve them, are discussed below.

- The use of lasers as light sources is expensive and introduces some speckle in the image. Although careful computational approaches can reduce this speckle, it is the opinion of the author that a minimal amount of speckle is unavoidable with lasers. Superluminescent, partially coherent light sources such as the latest generation of superluminescent LED's might represent a solution to this problem.
- Galvanometric scanners are cumbersome devices for scanning the Fourier plane. Practical implementations of the segmented scanning approach will probably use arrays of micromechanical deflectors such as those described in references 53 and 54. The use of these micromechanical components would eliminate most moving parts from the display (with the exception of the vertical scanner), thus rendering it essentially solid-state.
- Very large and expensive TeO_2 crystals will be required for large displays if the material is used in the shear mode. Using the same material in the longitudinal mode along with higher bandwidth electronics might prove more practical.

It is the opinion of the author that future developments in three-dimensional display technologies will benefit from more advanced studies in the psychophysics of human perception. The display developed in the context of this thesis should prove an ideal tool for psychophysical experiments

since it allows for an unprecendented control over three-dimensional imaging parameters and produces high quality images of a useful size.

More importantly, holographic video represents a truly new medium, a rare happening in human history. The relationship between electronic holography and still holography is similar to the relationship between television and still photography. These two types of holography will almost certainly evolve in quite different directions, each medium developing its own language. Some applications of electronic holography such as medical imaging, air trafic control, or car design are relatively straightforward , but it could be that the most interesting uses of an interactive holographic medium lie in an entirely different domain. The first medium to have been designed from the beginning as entirely digital, electronic holography permits the creation of arbitrary wavefronts, including some that do not exist in nature. It could thus have an impact in the visual arts comparable to the advent of electronic synthesizers (which create arbitrary sound waveforms) in music.

The prospects look bright for the future of holographic video displays. Our information processing capabilities have been growing exponentially over the last few decades and that growth shows no sign of slowing down with such technologies as optical computers, superconducting devices and ultra-fast semiconductors looming in the future. Some of the figures given in this thesis which seem a little bit farfetched now will be commonplace when a whole CHEOPS fits on a single chip. There is no doubt in the mind of the author that some kind of holographic display will one day be used for practical purposes. Whether this hypothetical device will use the current approach or will function on a totally different principle is harder to predict. The present system with its cumbersome electromechanical scanning array might one day be remembered as the late 20^{th} century equivalent of the Nipkow disk, but one thing is certain: it has carved itself a niche in scientific history as the first functional holographic video display.

APPENDIX A : The paraxial optical system with time dependent elements

A.1 Introduction

Optical scientists are well acquainted with the ABCD matrix description of the general paraxial optical system. Although very useful, this formalism cannot be directly used in the case of time-dependent systems, i.e. systems in which the rays are altered in a time-dependent fashion. Such systems are now becoming commonplace with the advent of laser scanning ans adaptive optics technologies. In this paper I will introduce an extension of the ABCD matrix formalism which will allow us to deal efficiently with time-dependent systems.

A.2 Problem Definition

A general paraxial optical system can be described by a set of linear equations which relate the positions x_1, x_2 and the slopes x'_1, x'_2 at any two reference planes:

$$\begin{aligned} x_2 &= Ax_1 + Bx'_1 \\ x'_2 &= Cx_1 + Dx'_1 \end{aligned} \tag{A.1}$$

Or, in matrix form:

$$\begin{bmatrix} x_2 \\ x'_2 \end{bmatrix} = \begin{bmatrix} A & B \\ C & D \end{bmatrix} \begin{bmatrix} x_1 \\ x'_1 \end{bmatrix} \tag{A.2}$$

we are now interested to investigate the case where the rays are affected in a time dependent fashion. That is, they can be translated or rotated by time dependent operators, as opposed to the pre-

vious case where all the components of the system were considered static. For a translation, Equation (A.1) thus becomes:

$$\begin{aligned} x_2 &= Ax_1 + Bx'_1 + Ht \\ x'_2 &= Cx_1 + Dx'_1 \end{aligned} \tag{A.3}$$

And for a rotation they become:

$$\begin{aligned} x_2 &= Ax_1 + Bx'_1 \\ x'_2 &= Cx_1 + Dx'_1 + Wt \end{aligned} \tag{A.4}$$

Obviously our ABCD matrices are no longer sufficient to describe the situation. The solution to this problem is to switch to a 3-dimensional space where a vector is now represented by the coordinates (x,x',t). If we neglect the propagation time for a ray, we will be now working in a plane imbedded in a larger 3-D space. This plane is defined by the time coordinate itself which does not change thorough the transformations. Such coordinates are called homogeneous coordinates. Thus a time dependent translation is now represented by the matrix:

$$\begin{bmatrix} x_2 \\ x'_2 \\ t \end{bmatrix} = \begin{bmatrix} 1 & 0 & H \\ 0 & 1 & 0 \\ 0 & 0 & 1 \end{bmatrix} \begin{bmatrix} x_1 \\ x'_1 \\ t \end{bmatrix} \tag{A.5}$$

And a rotation is represented by:

$$\begin{bmatrix} x_2 \\ x'_2 \\ t \end{bmatrix} = \begin{bmatrix} 1 & 0 & 0 \\ 0 & 1 & W \\ 0 & 0 & 1 \end{bmatrix} \begin{bmatrix} x_1 \\ x'_1 \\ t \end{bmatrix} \tag{A.6}$$

The general case can now be described by the matrix:

$$\begin{bmatrix} x_2 \\ x'_2 \\ t \end{bmatrix} = \begin{bmatrix} 1 & 0 & H \\ 0 & 1 & W \\ 0 & 0 & 1 \end{bmatrix} \begin{bmatrix} x_1 \\ x'_1 \\ t \end{bmatrix} \tag{A.7}$$

where A,B,C and D represent the coefficients of the traditional 2 x 2 ABCD matrices.

A.3 Examples

A.3.1 A Translating Thin Lens

Let us now consider the case of a thin lens translating at a speed H. We want to find the relationship between two references planes situated at distances l_1 in front and l_2 in back of the lens.

A thin lens is represented by the matrix:

$$M_1 = \begin{bmatrix} 1 & 0 & 0 \\ \frac{-1}{f} & 1 & 0 \\ 0 & 0 & 1 \end{bmatrix} \tag{A.8}$$

We now consider this lens moving at a speed H with respect to the rest of the system. This means that the coordinate system of the lens will change over time. In the original reference frame, such a translation will be represented by the product:

$$M_2 = T^{-1} M_1 T \tag{A.9}$$

where T is the translation matrix of equation (A.5). After calculation we get the result:

$$M_2 = \begin{bmatrix} 1 & 0 & 0 \\ \frac{-1}{f} & 1 & \frac{H}{f} \\ 0 & 0 & 1 \end{bmatrix} \tag{A.10}$$

We thus conclude that a lateral translation of a lens results in an angular ray displacement. To have the general matrix relating two arbitrary reference planes we then multiply by the matrices corresponding to the propagation of the rays in free space:

$$M = \begin{bmatrix} 1 & l_2 & 0 \\ 0 & 1 & 0 \\ 0 & 0 & 1 \end{bmatrix} \begin{bmatrix} 1 & 0 & 0 \\ \frac{-1}{f} & 1 & \frac{H}{f} \\ 0 & 0 & 1 \end{bmatrix} \begin{bmatrix} 1 & l_1 & 0 \\ 0 & 1 & 0 \\ 0 & 0 & 1 \end{bmatrix}$$

$$= \begin{bmatrix} 1-\frac{l_2}{f} & l_1 + l_2\left(1-\frac{l_1}{f}\right) & H\frac{l_2}{f} \\ -\frac{1}{f} & 1-\frac{l_1}{f} & \frac{H}{f} \\ 0 & 0 & 1 \end{bmatrix} \tag{A.11}$$

If the light source is positioned at l_1 and l_2 describes image position the matrix becomes:

$$M = \begin{bmatrix} -\frac{l_2}{l_1} & 0 & H\frac{l_2}{f} \\ -\frac{1}{f} & -\frac{l_1}{l_2} & \frac{H}{f} \\ 0 & 0 & 1 \end{bmatrix} \tag{A.12}$$

A.3.2 A traveling image on a Bragg cell

A holographic image travelling on a Bragg cell can be considered of consisting of a multitude of superimposed lenslets, each of which images a specific point in the image space (superposition principle). If the Bragg cell is illuminated by a plane wave (which is usually the case in practice) and we consider the case of a particular point imaged at a distance d_0 from the Bragg cell the matrix formulation becomes:

$$\begin{bmatrix} x_1 \\ x'_1 \\ t \end{bmatrix} = \begin{bmatrix} 1 & l_1 \to \infty & 0 \\ -\frac{1}{d_0} & l_1 \to \infty & \frac{V}{d_0} \\ 0 & 0 & 1 \end{bmatrix} \begin{bmatrix} x_0 \\ 0 \\ t \end{bmatrix} = \begin{bmatrix} x_0 \\ \frac{(-x_0 + Vt)}{d_0} \\ t \end{bmatrix} \tag{A.13}$$

A.3.3 A scanning mirror

A scanning mirror rotating at an angular rate ω deflects an incoming beam at a rate 2ω. Its matrix is thus of the form:

$$M = \begin{bmatrix} 1 & 0 & 0 \\ \frac{-1}{f} & 1 & 2\omega \\ 0 & 0 & 1 \end{bmatrix} \tag{A.14}$$

A.4 Analysis of Scophony-type displays

We now posess all the elements necessary to model an optical system similar to the one used in the MIT electronic holography display. Such a system is represented schematically in Figure A.1.

The Bragg cell is illuminated from point source S_1 located on axis. Each image component displayed at a specific depth d_0 with respect to the Bragg cell can be modeled as a series of diffractive lenslets having a focal length d_0. In defining d_0 we use the usual sign convention, i.e. d_0 is negative if the lenslet is diverging and positive if it is converging. It is sufficient to track the behavior of the

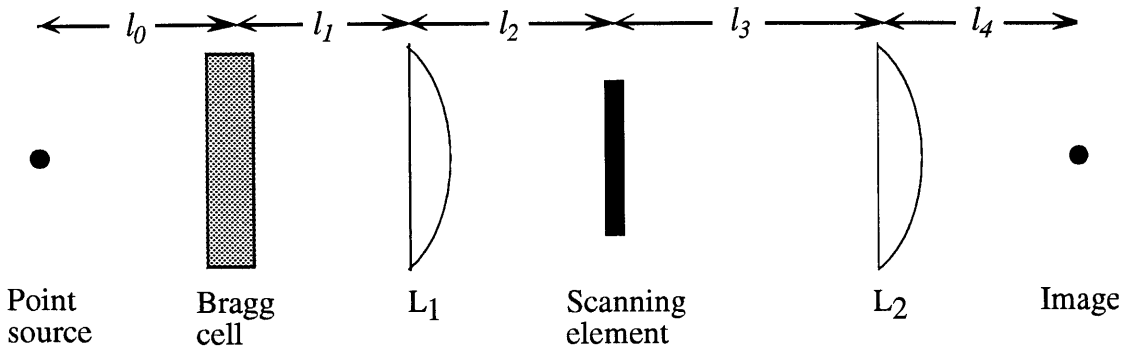

Figure A.1 Schematic diagram of a Scophony-type optical system

light interacting with a single lenslet to deduce the behavior of the system with respect to different planes.

By using the previously described formalism the whole system can be modeled as the product:

$$\begin{bmatrix} x_{out} \\ x'_{out} \\ t \end{bmatrix} = M_{system} \begin{bmatrix} x_{in} \\ x'_{in} \\ t \end{bmatrix} \tag{A.15}$$

with

$$M_{system} = M_8 M_7 M_6 M_5 M_4 M_3 M_2 M_1 M_0 \tag{A.16}$$

and the corresponding matrices described as:

$$M_0 = \begin{bmatrix} 1 & l_0 & 0 \\ 0 & 1 & 0 \\ 0 & 0 & 1 \end{bmatrix} \tag{A.17}$$

$$M_1 = \begin{bmatrix} 1 & l_0 & 0 \\ \frac{-1}{d_0} & 1 & \frac{V}{d_0} \\ 0 & 0 & 1 \end{bmatrix} \tag{A.18}$$

where V represents the acoustic propagation rate on the Bragg cell.

$$M_2 = \begin{bmatrix} 1 & l_1 & 0 \\ 0 & 1 & 0 \\ 0 & 0 & 1 \end{bmatrix} \tag{A.19}$$

$$M_3 = \begin{bmatrix} 1 & 0 & 0 \\ \frac{-1}{f_1} & 1 & 0 \\ 0 & 0 & 1 \end{bmatrix} \tag{A.20}$$

$$M_4 = \begin{bmatrix} 1 & l_2 & 0 \\ 0 & 1 & 0 \\ 0 & 0 & 1 \end{bmatrix} \tag{A.21}$$

$$M_5 = \begin{bmatrix} 1 & 0 & 0 \\ 0 & 1 & 2\omega \\ 0 & 0 & 1 \end{bmatrix} \tag{A.22}$$

$$M_6 = \begin{bmatrix} 1 & l_3 & 0 \\ 0 & 1 & 0 \\ 0 & 0 & 1 \end{bmatrix} \tag{A.23}$$

$$M_7 = \begin{bmatrix} 1 & 0 & 0 \\ -\frac{1}{f_2} & 1 & 0 \\ 0 & 0 & 1 \end{bmatrix} \tag{A.24}$$

$$M_8 = \begin{bmatrix} 1 & l_4 & 0 \\ 0 & 1 & 0 \\ 0 & 0 & 1 \end{bmatrix} \tag{A.25}$$

For the display to render a steady image the following conditions must be met:

- The conventional imaging criterion must be observed. This is equivalent to stating that the first row, second column element $M^{12}$of M_{system} (the B of the subset ABCD matrix) is nul:

$$M_{system}^{12} = 0 \tag{A.26}$$

- The image must be steady in the image plane. This can be stated as:

$$\frac{dx_{out}}{dt} = 0 \tag{A.27}$$

where x_{in} denotes the position of the source S.

- The spatial frequencies of the lenslet written on the Bragg cell must be time independent in the image plane. This is equivalent to state that the chief ray of the source and moving lenslet sub-system must be mapped to a time-independant ray in the image space. This condition can be stated as:

$$\frac{dx'_{out}}{dt} = 0 \tag{A.28}$$

with

$$x'_{in} = \frac{Vt}{l_0} \tag{A.29}$$

Finding a correct imaging system is thus equivalent to applying applying the previous conditions on equation (A.15) where the input vector $\vec{x}_{in}$ is given by:

$$\vec{x}_{in} = \begin{bmatrix} x_0 \\ \frac{Vt}{d_0} \\ t \end{bmatrix} \tag{A.30}$$

Such a calculation can be done analytically by using mathematical programs such as *Mathematica*. However, calculations done using the general matrix of expression (A.16) results in formidably long expressions for the desired quantities. These expressions can be significantly shortened if the light source is placed at infinity (which is usually the case in practice) and if the Bragg cell is placed against lens L_1 (thus $l_1 = 0$), which also has the advantage of rendering the display more compact. In that case the application of conditions (A.27) and (A.28) on the image vector gives the expressions:

$$\frac{dx_{out}}{dt} = \frac{V}{d_0}\left(l_2 + l_3 + l_4 - l_4\left(\frac{l_2 + l_3}{f_2}\right)\right) + 2\omega\left(l_3 + l_4 - \frac{l_3 l_4}{f_2}\right) = 0 \tag{A.31}$$

$$\frac{dx'_{out}}{dt} = \frac{V}{f_1 f_2}(l_2 + l_3 - f_1 - f_2) + 2\omega\left(1 - \frac{l_3}{f_2}\right) \tag{A.32}$$

The variable l_4 of (A.31) can be substituted by using condition (A.26). Solving for l_2 then results in the expression:

$$l_2 = \frac{f_1(V + 2\omega d_0)}{2\omega(d_0 + f_1)} \tag{A.33}$$

And solving (A.32) for l_3 gives the result:

$$l_3 = f_2 + \frac{V(f_1 - l_2)}{V - 2\omega f_1} \tag{A.34}$$

The magnification of the holographic image can be determined by considering the projection of the lenslet foci plane (situated at a distance d_0 from L_1 if the source is at infinity) by lenses L_1 and L_2. Such a calculation can be done with conventional ray optics to give the result:

$$M_t = \frac{f_1 f_2}{f_1 f_2 + d_0(f_1 + f_2) - (l_2 + l_3)(d_0 + f_1)} \tag{A.35}$$

APPENDIX B: Demonstration of equation (4.6).

The optical system under consideration consists of a point source S, an aperture stop P, an imaging lens L_1 and the pupil of the eye P_{eye}(Figure B.1). The pupil P is situated at the front focal plane of L_1 (such a system is said to be *telecentric on the image side.*). We want to find the minimum size d_0 of P that will prevent vignetting.

The exit pupil of the first section of the system is determined by projecting the geometrical shadow of P on he plane of lens L_1:

$$d_1 = \frac{d_0 l_1}{l_0} = \frac{d_0 l_1}{l_1 - f_1} \tag{B.1}$$

and the non vignetting condition can be expressed as:

$$d_1 > \frac{d_{eye} l_2}{l_3} \tag{B.2}$$

From the lens law we have:

$$l_1 = \frac{f_1 l_2}{l_2 - f_1} \tag{B.3}$$

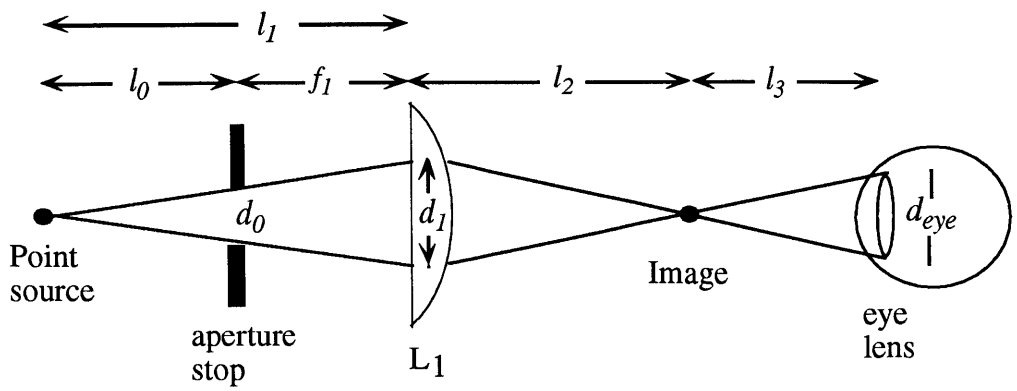

Figure B.1 Telecentric imaging system

Substituting (B.3) into (B.1) yields the result:

$$d_1 = \frac{d_0 l_2}{f_1} \tag{B.4}$$

and thus condition (B.2) can be expressed as:

$$d_0 > \frac{d_{eye} f_1}{l_3} \tag{B.5}$$

APPENDIX C: Sync circuitry

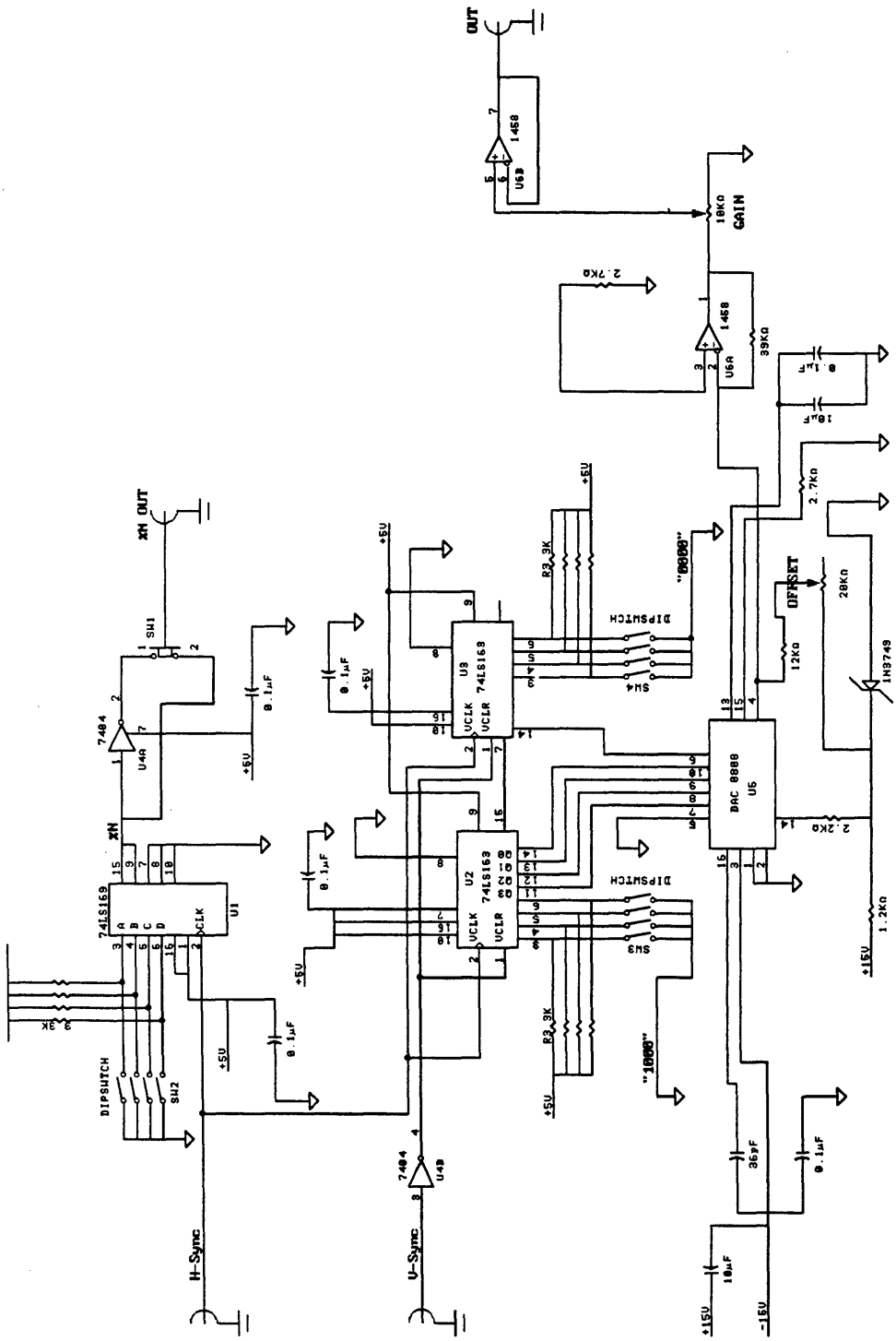

REFERENCES

1. P. St Hilaire, S.A. Benton, M. Lucente, M. L. Jepsen, J Kollin, H. Yoshikawa, "Electronic Display System for Computational Holography", in SPIE Proceedings #1212 "Practical Holography IV", (SPIE, Bellingham, WA, 1990), S.A. Benton, editor, pp 174-182.

2. P. St Hilaire, M. Lucente, S. A. Benton, "Synthetic Aperture Holography: A Novel Approach to Three Dimensional Displays", Journal of the Optical Society of America A, Vol. 9, No. 11, Nov. 1992, pp 1969 - 1977.

3. M. Lucente, P. St Hilaire, S. A. Benton, D. Arias, J. A. Watlington, "New Approaches to Holographic Video", SPIE Proceedings #1732 "Holography '92", (SPIE, Bellingham, WA, 1992), paper #1732-48.

4. E. Leith, J. Utpatnieks, K. Hildebrand and K. Haines, "Requirements for a Wavefront Reconstruction Television Facsimile System". J. SMPTE, Vol. 74, pp. 893-896 (1965).

5. I. C. Chang, "Acoustooptic Devices and Applications", *IEEE transactions on sonics and ultrasonics,* vol. su-23, No. 1, January 1976.

6 A. Korpel, "Acousto-Optics-A review of Fundamentals", *Proceedings of the IEEE,* vol. 69, No 1, January 1981.

7. L. Bademian, "Parallel-Channel Acousto-Optic Modulation", *Optical Engineering,* vol. 25, pp 303-308, Feb 1986.

8. A. Vanderlugt *et al.*, "Multichannel Bragg Cells: Compensation for Acoustic Spreading", *Applied Optics,* vol. 22, pp 3906-3912, Dec. 1983.

9. W. J. Dallas, "Computer Generated Holograms", in The Computer in Optical Research, B. R. Frieden editor, Vol. 41 of Springer Series in Applied Physics, (Springer Verlag, Berlin, (1980), pp. 291-366.

10. G. Tricoles, "Computer Generated Holograms: a Historical Review", Applied Optics, Vol. 26, pp. 4351-4360 (1987).

11. E. Leith, J. Utpatnieks, K. Hildebrand and K. Haines, "Requirements for a Wavefront Reconstruction Television Facsimile System". J. SMPTE, Vol. 74, pp. 893-896 (1965).

12. Enloe, Murphy and Rubinstein, "Hologram Transmission via Television", Bell System Tech. Jour. 1, pp. 335-339, February 1966.

13. Burckhardt and Enloe, "Television Transmission of Holograms with Reduced Resolution Requirements on the Camera Tube", Bell System Tech. Jour., Vol. XXX, pp 1529-1535, May-June 1969.

14. S.A. Benton, "The Mathematical Optics of White Light Transmission Holograms", in Proceedings of the First International Symposium on Display Holography, Lake forest College, July 1982, T.H. Jeong, editor.

15. S.A. Benton, "Experiments in holographic video" , in SPIE Proceedings on holography - Commemorating the 90th anniversary of the birth of Dennis Gabor, Vol. IS-8 (SPIE, Bellingham, WA 1991), pp. 247-267.

16. L. M. Myers, "The Scophony system: an analysis of its possibilities.", TV and Shortwave World, pp 201-294, April 1936.

17. J. Sieger, J.H. Jeffree, "Improvements in or relating to Light Modulating Devices and to Electrical Circuits to use therewith", British Patent #482665.

18. A. Korpel, R. Adler, P. Desmares, and W. Watson, "A Television Display Using Acoustic Deflection and Modulation of Coherent Light", Applied Optics, vol. 5, pp. 1667-1682, October 1966.

19. M. Lucente, "Optimization of Hologram Computation for Real Time Display" to be published in SPIE Proceedings #1667 "Practical Holography VI", (SPIE, Bellingham, WA, 1992), S.A. Benton, editor.

20. A. Goutzoulis and I. Abramovitz, "Digital Electronics Meets Its Match", IEEE Spectrum, pp 21-25, August 1988.

21. N.J. Berg and J.N. Lee eds. "Acousto-optic Signal Processing Theory and Implementation", Vol. 2 of Optical Engineering Series, (Marcel Dekker, New York, 1983).

22. L. Beiser, "Laser Scanning Systems", in Laser applications Vol. 2, (Academic Press, San Diego, 1974), p. 53-155.

23. I. C. Chang, "Acoustooptic Devices and Applications", IEEE transactions on sonics and ultrasonics, vol. su-23, No. 1, pp 2-22, January 1976.

24. R.E. Hopkins and M.J. Buzawa, "Optics for Laser Scanning", Optical Engineering, vol. 15, pp. 90-94, April 1976.

25. P. St-Hilaire, S.A. Benton, M. Lucente, J. Underkoffler, H. Yoshikawa, "Real-time holographic display: Improvements using a multichannel acousto-optic modulator and holographic optical elements", SPIE Proceedings #1461 "Practical Holography V", (SPIE, Bellingham, WA, 1991), S.A. Benton, editor, pp. 254-261.

26. W. Parker, "Output Devices for Dynamic Electronic Holography", Master's thesis, MIT Media Laboratory, February 1989.

27. J. Kollin, "Design and Information Considerations for Holographic Television", Master's thesis, MIT Media Laboratory, June 1988.

28. M.L. Jepsen, "Holographic Video: Design and Implementation of a Display System", Masters thesis, MIT Media Laboratory, June 1989.

29. G. Goetz, K. Mueller, D. Shupe, "Recent Progress in a Real Time Three-Dimensional Display", *IEEE trans. Elec. Devices*, Vol. ED-20, No 11, 1973.

30. W.F. Schreiber, "Fundamentals of Electronic Imaging Systems", Springer-Verlag, 1986.

31. C.V. Raman and N.S.N. Nath, *Proceedings of the Indian Academy of Sciences*, vol. 2, p 406, 1935.

32. A. Korpel, "Acousto-Optics", Marcel Dekker, 1988.

33. G.J. Swanson, "Binary Optics Technology: The Theory and Design of Multi-Level Diffractive Optical Elements", *MIT Lincoln Laboratory technical report 854*, August 1989.

34. P. St-Hilaire, S.A. Benton *et al.*, "Real-time holographic display: Improvements using a multichannel acousto-optic modulator and holographic optical elements", *SPIE Proceedings*, Vol. #1461 "Practical Holography V", 1991, S.A. Benton, editor.

35. P. St Hilaire "Real-Time Holographic Display: Improvements Using Higher Bandwidth Electronics and a Novel Optical Configuration", S.M Thesis, Media Arts and Sciences Section, Massachussetts Institute of Technology, June 1990.

36. P. St. Hilaire, "Modulation Transfer Function and Optimum Sampling of Holographic Stereograms", accepted for publication in Applied Optics.

37. N. Hashimoto, S. Morokawa, K. Kitamura, "Teal Time Holography using the High-Resolution LCTV-SLM.", in SPIE Proceedings #1461 "Practical Holography V", (SPIE, Bellingham, WA, 1991), S.A. Benton, editor, pp 291-302.

38. S. A. Benton, P. St. Hilaire, M. Lucente, J. D. Sutter, W. J. Plesniak, "Real Time Computer Generated 3-D Holograms", SPIE Proceedings #1983 "16th Congress of the International Comission for Optics", (SPIE, Bellingham, WA, 1993), pp 536 - 543.

39. P. St. Hilaire, S. A. Benton, M. Lucente, J. D. Sutter, W. J. Plesniak, "Advances in Holographic Video", SPIE Proceedings #1914 "Practical Holography VII", (SPIE, Bellingham, WA, 1993), paper #1914-27.

40. P. St. Hilaire, S. A. Benton, M. Lucente, P. M. Hubel, "Color Images with the MIT Holographic Video Display", SPIE Proceedings #1667 " Practical Holography VI", (SPIE, Bellingham, WA, 1992), paper #1667-33.

41. A. Bardos, Appl. Opt. 13, 832 (1974).

42. D. R. Pape, "Multichannel Bragg Cells: design, performance, and applications.

43. A. VanderLugt, "Bragg cell diffraction patterns", Appl. Opt. 21, pp 1092-1100 (1982).

44. M.G. Cohen, "Optical study of ultrasonic diffraction and focussing in anisotropic media", J. Appl. Phys. 38(10), 3821 (1967).

45. J. Randolph and J. Morrison, "Modulation transfer function of Bragg cells", Appl. Opt. 10, pp. 1383-1387, (June 1971).

46. V. M. Bove Jr and J. A. Watlington, "Cheops: a modular processor for scalable video coding", in Proceedings of SPIE Visual communications and Image Processing '91 conference, (SPIE, Bellingham, WA, 1991), Nov. 1991.

47. D. L. Arias, "Design of an 18 channel framebuffer for holographic video" S.B. thesis, MIT EECS department, Feb. 1992.

48. D. Psaltis, E.G. Paek, and S.S. Venkatesh, Opt. Eng. 23, 698 (1984).

49. F. Mok, J. Diep, H.K. Liu, D. Psaltis, "Real-time computer generated hologram by means of liquid-crystal television spatial light modulator", Opt. Lett. 11, 748-750, Nov. 1986.

50. H. A. Haus, "Waves and fields in optoelectronics", Prentice Hall series in solid-state physical electronics, Prentice-Hall, NJ, pp 132-136.

51. J.W. Goodman, "Introduction to Fourier Optics", McGraw Hill Book Co., San Francisco, pp. 101-133 (1968).

52. T. Kaneko and A. Ishii, "One dimensional hologram recording using an acousto-optic deflector", Electronics and communications in Japan, Vol. 62-C, No. 4, pp 112-121, 1979.

53. M.G. Allen, M. Scheidl, R. Smith, A.D. Nikolich, "Movable micromachined silicon plate with integrated position sensing", Sensors and Actuators, A21-A23 (1990), pp 211-214.

54. K.E. Petersen, "Silicon torsional scanning mirror", IBM J. Res. Develop, Vol. 24, No 5, Sept 1980, pp 631-637.

55. J. S. Kollin, S.A. Benton, M.L. Jepsen, "Real-Time Display of 3-D Computed Holograms by Scanning the Image of an Acousto-Optic Modulator" in G. M. Morris, ed., SPIE Proc. Vol. #1136, Holographic Optics II: Principles and Applications (Soc. Photo-Opt. Instr. Engineers, Bellingham, WA, 1989), paper #1136-60.

56. R.V. Johnson, "Electronic Focusing in the Scophony Scanner", SPIE Vol. 222 Laser Scanning and Recording for Advanced Image and Data Handling", (Soc. Photo-Opt. Instr. Engineers, Bellingham, WA, 1980), pp 15-18.

57. Jeffree, J.H. , "Modulateur de lumiere", French patent No. 786,641 (1935).

58. S.A. Benton and J.S. Kollin, "Three-Dimensional Display System", U.S. Patent 5,172,251 (issued December 15, 1992; filed April 20, 1990).

59. S.A. Benton, "Experiments in Holographic Video", in P. Greguss and T.J. Jeong, eds. , SPIE Proc Vol. #IS-8, SPIE Institute on Holography, June 1990, pp. 247-267.

60. G. Colby and L. Scholl, "Transparency and Blur as Selective Cues for Complex Visual Information", in W. Bender, ed., SPIE Proc. Vol. #1460 (Soc. Photo-Opt. Instr. Engineers, Bellingham, WA, 1991), paper #1460-13, pp. 114-134.

61. T Matsuishi, D. Small, R. L. MacNeil, "6K x 2K Display Prototype", SPIE Proc. Vol. #1664, High resolution displays and projection systems, (Soc. Photo-Opt. Instr. Engineers, Bellingham, WA, 1989), paper #1664-27.

62. E. H. Adelson and J. R. Bergen, "The Plenoptic Function and the Elements of Early Vision", in Computational Models of Visual Processing, M. Landy and J.A. Morshon eds., MIT Press, 1991.

63. R.C. Emerson, J.R. Bergen, E.H. Adelson, "Movement models and directionally selective neurons in the cat's visual cortex", Society for Neuroscience Abstracts, 13, 1623 (1987).

64. L.J. Cutrona *et al.*, "On the application of coherent optical processing techniques to synthetic-aperture radar", Proc IEEE 54:1026 (1966).

65. K.M. Carson, "A Color Spatial Display Based on a Raster Framebuffer and Varifocal Mirror", Master's thesis, MIT Media Laboratory, February 1985.